

THE SCHÜTZENBERGER INVOLUTION AND COLORED LATTICE MODELS

HENRIK P. A. GUSTAFSSON AND CARL WESTERLUND

ABSTRACT. Colored lattice models can be used to describe many different types of special functions of interest in both algebraic combinatorics and representation theory, for example Schur polynomials, nonsymmetric Macdonald polynomials, and characters and Whittaker functions for representations of p -adic groups. A notable example is the metaplectic ice model of which there are actually two different variants: a Gamma and a Delta variant. These variants differ in key aspects but surprisingly produce equal partition functions, which are weighted sums over admissible configurations, and this equality is called the Gamma-Delta duality. The duality was used to prove the analytic continuation of certain multiple Dirichlet series and is highly non-trivial, especially since the number of configurations on each side of the equality can differ.

In this paper we construct a new family of solvable, colored lattice models and prove that they are dual to existing lattice models in the literature, including the above metaplectic case and the lattice model for (non-metaplectic) Iwahori Whittaker functions together with its crystal limit for Demazure atoms for Cartan type A . The equality of partition functions is shown using Yang–Baxter equations involving R -matrices mixing lattice model rows of types Gamma and Delta.

For the crystal Demazure lattice model we show that the duality refines to a weight-respecting bijection of states given by the Schützenberger involution on the associated Gelfand–Tsetlin patterns or semistandard Young tableaux. We also show how the individual steps exchanging two rows in the proof of the duality for the partition functions refines to Berenstein–Kirillov, or Bender–Knuth involutions.

2020 *Mathematics Subject Classification.* Primary: 82B23 Secondary: 16T25, 05E10, 05A19, 05E05.

Key words and phrases. Solvable lattice models, Gamma-Delta duality, Gelfand–Tsetlin patterns, Berenstein–Kirillov involutions, Schützenberger involutions.

CONTENTS

1.	Introduction	2
2.	The families of lattice models	6
2.1.	Setup	6
2.2.	Fusion and boundary conditions	7
2.3.	Specializations	10
2.4.	Crystal models	12
3.	Solvability and Yang–Baxter equations	14
3.1.	Remarks about quantum groups	22
3.2.	Solvability of the crystal model	23
3.3.	From Γ - Δ duality to left-right duality	24
4.	Crystal models and the Schützenberger involution	28
4.1.	Gelfand–Tsetlin patterns	28
4.2.	Berenstein–Kirillov involutions	32
4.3.	Proof of Theorem 4.10	38
Appendix A. Proof of Proposition 3.4		46
References		49

1. INTRODUCTION

The main focus of this paper is the construction of a new family of solvable, colored lattice models and showing that it is dual to the family of lattice models in [BBBG24b]. By *dual* we mean that they give the same partition functions, which are functions in the row parameters $\mathbf{z} = (z_1, \dots, z_r)$. Both families of lattice models consist of configurations, or states, of colored paths through a two-dimensional grid, but an important difference is that in the new family the paths are only moving in the directions down and left, while in the previous family they are moving down and right. The two families are not simply mirror images of each other; indeed proving that their partition functions are equal is highly non-trivial and the two partition functions may involve a different number of states.

The partition functions of colored lattice models have been used in several papers [BBBG21, BBBG24a, BBBG24c] to describe special functions in representation theory such as characters and Whittaker functions of p -adic representations. For this paper the representation theoretic origins of the lattice models will not be important for our arguments, but we present them here as a motivation. From the viewpoint of algebraic combinatorics, these colored lattice models produce for example Schur polynomials and limits of Macdonald polynomials with prescribed symmetry. For other lattice models producing nonsymmetric Macdonald polynomials see [BW22].

Two important cases of colored lattice models are those describing so-called Iwahori Whittaker functions and metaplectic spherical Whittaker functions of Cartan type A . We sometimes call these lattice models Iwahori ice and metaplectic ice because of their resemblance to historical six-vertex models used to describe ice. The former was constructed in [BBBG24a] while the latter was originally constructed in [BBC⁺12, BBB19] using a different description but later recast as a colored lattice model in [BBBG24b].

The family of right-moving lattice models from [BBBG24b] was constructed to interpolate between the Iwahori and metaplectic ice models through Drinfeld twists of the underlying affine supersymmetric quantum group $U_q(\widehat{\mathfrak{gl}}(m|1))$ where m is the number of colors. It was used in [BBBG24b] to prove that the two seemingly very different types of Whittaker functions described above are actually equal and this identity was called the *Iwahori-metaplectic duality*.

Another important feature that was used to prove this equality was that there are actually two variants of metaplectic ice called Γ and Δ which are left- and right-moving, respectively, and that these two variants give the same partition functions. This equality of the Γ and Δ variants, called the Γ - Δ duality, was originally used to prove the analytic continuation and functional equations of so-called Weyl group multiple Dirichlet series in [BBF11b, BBB19, BBBG17].

The existence of these two variants for the metaplectic ice model suggested to us that there should be a left-moving variant of Iwahori ice as well, and in fact a whole family of left-moving lattice models dual to the right-moving family as visualized in Figure 1. Indeed, we now prove that in this paper.

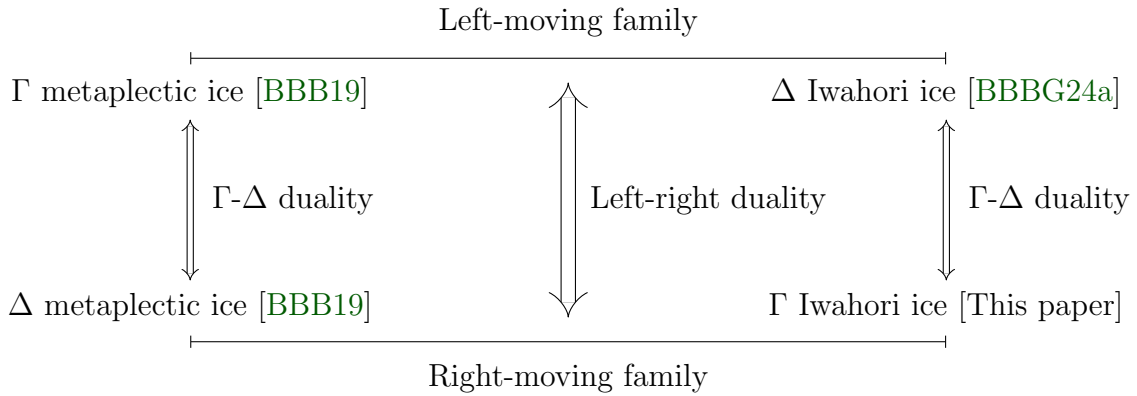


Figure 1. The left- and right-moving families of lattice models together with their specializations, naming conventions and references.

We also prove that the whole family is *solvable*, meaning that it satisfies Yang–Baxter equations including those that mix left- and right-moving models. The proof is self-contained and implies in particular the (mixed and non-mixed) Yang–Baxter equations for the known Iwahori ice model and both variants of the metaplectic ice models. The mixed Yang–Baxter equations are then used to prove that the left- and right-moving families are dual using the familiar *train argument* which swaps two rows of the lattice models.

An important motivation for the work in this paper was, as mentioned, to find a left-moving dual to Iwahori ice. We plan to use this in a future project to prove a generalized version of the Iwahori-metaplectic duality for Whittaker functions which are both simultaneously metaplectic and Iwahori invariant. The left-moving Iwahori model is also expected to be used to construct a lattice model for Iwahori Whittaker functions of types B and C by alternating left- and right-moving rows.

Another important result of this paper is that the left-right duality refines to a weight-respecting left-right bijection of the states for a particular limit of the parameters of the families: first we specialize to the left- and right-moving Iwahori ice models and then we take the so-called crystal limit $v \rightarrow 0$ of a parameter v . In this limit the states are naturally

in bijection with Gelfand–Tsetlin patterns and therefore also semistandard Young tableaux (SSYT) on which the left-right bijection becomes the Schützenberger involution. The weight of the state is then given by $\mathbf{z}^{\text{wt}(T)}$ where $\text{wt}(T)$ is the weight of the corresponding tableau. In [BBBG21], Gustafsson and collaborators showed that the right-moving crystal model describes Demazure characters of Cartan type A and we thus get a new left-moving lattice model for these characters in this paper.

As mentioned above, the proof of the left-right duality for partition functions uses Yang–Baxter equations to swap pairs of adjacent rows. We show that these row swaps can be refined by Berenstein–Kirillov involutions t_i on Gelfand–Tsetlin patterns introduced in [KB95], or Bender–Knuth involutions BK_i on SSYT introduced in [BK72], which act on the weight by a simple transposition. The way the left-right duality reduces into individual row swaps mirrors the factorization of the Schützenberger involution into Berenstein–Kirillov involutions.

To summarize, we get the following commuting diagram which is weight-respecting, meaning that the associated weights transform by the corresponding simple transposition,

$$\begin{array}{ccccc}
\mathfrak{S}_{\lambda+\rho}^{\Theta} & \longleftrightarrow & \text{GTP}_{\lambda} & \longleftrightarrow & \text{SSYT}(\lambda) \\
\updownarrow & & \updownarrow t_{r-i} & & \updownarrow \text{BK}_{r-i} \\
\mathfrak{S}_{\lambda+\rho}^{s_i\Theta} & \longleftrightarrow & \text{GTP}_{\lambda} & \longleftrightarrow & \text{SSYT}(\lambda)
\end{array}$$

Here $\text{SSYT}(\lambda)$ is the set of semistandard Young tableaux with shape $\lambda = (\lambda_1, \dots, \lambda_r) \in \mathbb{Z}^r$, where $\lambda_1 \geq \dots \geq \lambda_r \geq 0$, and GTP_{λ} is the set of Gelfand–Tsetlin patterns with top row λ . Lastly, $\mathfrak{S}_{\lambda+\rho}^{\Theta}$ denotes the set of states of the lattice model with (a mix of) left- and right-moving rows given by Θ , such that $\Theta_i \neq \Theta_{i+1}$, and $\lambda + \rho$, where $\rho = (r-1, r-2, \dots, 1, 0)$, denotes which column numbers have top boundary edges occupied by paths.

As an intermediate step we define subsets of Gelfand–Tsetlin patterns where different pairs of consecutive rows are either so-called left-strict or right-strict matching the row types of the lattice model. We show the combinatorial result that Berenstein–Kirillov involutions act naturally on these subsets by swapping distinct row types.

For a crystal model with r rows we fix some r -tuple of colors for the top boundary edges. The r colored paths of a state then goes from the top boundary and exit on the left and right boundary at left- and right-moving rows respectively and we can keep track of these boundary colors by an r -tuple σ . Denoting the set of such states by $\mathfrak{S}_{\lambda+\rho, \sigma}^{\Theta}$ we show that the left-right bijection respects the horizontal boundary colors and descends to a bijection $\mathfrak{S}_{\lambda+\rho, \sigma}^{\Theta} \longleftrightarrow \mathfrak{S}_{\lambda+\rho, s_i\sigma}^{s_i\Theta}$. To prove this we show that σ is determined from the associated Gelfand–Tsetlin pattern using an action of the Coxeter monoid corresponding to the symmetric group S_r . This generalizes a similar statement in [BBBG21] to mixed states. We complete the proof by showing how σ transforms under Berenstein–Kirillov involutions using a combinatorial argument.

Addressing two questions in the literature. We will now address a question connected to the book [BBF11b] regarding *packets* of states and another question connected to the paper [BS22] regarding the crystal limit.

As mentioned above, the non-crystal duality between the left- and right-moving families cannot, in general, be refined to a bijection on states. This issue was studied in [BBF11b] for the metaplectic Γ and Δ case (in the language of Gelfand–Tsetlin patterns predating

the constructions of the corresponding lattice models). They empirically observed that the Gelfand–Tsetlin patterns could be partitioned into smaller *packets* which give a partial refinement of the duality, that is, that the partition functions of the packet and its dual agree.

For special subsets of Gelfand–Tsetlin patterns they showed in [BBF11b, Chapter 10] that the corresponding packets are singletons (thus reducing the metaplectic Γ - Δ duality to a bijection of states for these particular subsets).

Furthermore, they showed that the packets in a related *Statement E* are described using facets of a particular simplex, but it is unclear how this can be interpreted in terms of lattice models states.

Since the members of each lattice model family is related by a form of Drinfeld twisting, it would be natural to consider packets that are invariants for the whole family. The results of this paper for the crystal limit of the Iwahori specialization could then be an important piece of the puzzle.

Our results also address an important issue raised in [BS22]. In that paper they construct a lattice model describing Demazure character for Cartan types B and C consisting of alternating left- and right-moving rows called Δ and Γ respectively as well as a new type of vertex called a *cap* connecting two rows. The Γ and Δ vertex configurations and weights agree with the left- and right-moving crystal limits of the Iwahori models in this paper. The right-moving Γ variant was originally constructed in [BBBG21] which was later generalized to the Iwahori ice model originally defined in [BBBG24a].

Buciumas and Scrimshaw showed that their model in [BS22] is *quasi-solvable*, meaning that it satisfies Yang–Baxter equations using three (mixed) R -matrices. However they were unable to find a suitable fourth R -matrix required for full solvability. One reason for this that they mentioned was that there are internal loops of paths with colors not fixed by the boundary conditions in the Yang–Baxter equations (which are therefore summed over), seemingly resulting in an m -dependence on only one side of the equation.

For the families in this paper we have found all four R -matrices and show that they satisfy the corresponding Yang–Baxter equations. We show that the issue of color loops for the general family is resolved by the fact that the m -depending color loop sums are telescoping sums reducing to an expression that matches an m -dependence in the fourth R -matrix on the other side of the equation. However, when taking the crystal limit $v \rightarrow 0$ in the Iwahori specialization of our families, the missing fourth R -matrix of [BS22] becomes very degenerate with most vertex weights being zero, and in particular it loses the m -dependent factors.

This paper is organized as follows. We explain how the families of lattice models are constructed in Section 2 and how specializations of them relate to models previously defined in the literature. In Section 3 we introduce the different types of Yang–Baxter equations that are used in the paper and we prove that the families of lattice models satisfy these equations in Theorem 3.1. In the same section we also prove the duality of the left- and right-moving families, that is, show that their partition functions agree, in Theorem 3.10. Because of color loops, the fourth R -matrix mentioned above needs to be treated differently from the other cases. Although we do not need this particular R -matrix for the rest of our results, we show how the Yang–Baxter equations involving it can be reduced to the other cases without it in Section 3 and Appendix A. Lastly, we consider the crystal limit of the Iwahori models in Section 4 where we first show that there is a bijection between mixed states and Gelfand–Tsetlin patterns, define the Berenstein–Kirillov involutions and describe how

they give the Schützenberger involution. We show how the Berenstein–Kirillov involutions give a bijection of states of different mixed row types and, in Theorem 4.7, how the weight of the state is transformed. In Theorem 4.10 we then prove that the boundary colors of the state are transformed as expected using a combinatorial argument based on patterns of elements in a Coxeter monoid.

Acknowledgements. We would like to thank the participants of the *Conference on Solvable Lattice Models, Number Theory and Combinatorics* in Dublin 2024 for their comments on an early presentation of the results in this paper. We are particularly thankful to Ben Brubaker and Daniel Bump as well as Valentin Buciumas and Travis Scrimshaw for helpful discussions about their work [BBF11b] and [BS22].

2. THE FAMILIES OF LATTICE MODELS

2.1. Setup. Consider a rectangular grid with r rows and N columns, which we will think of as a graph with the crossings as vertices. There are edges at the boundary of the grid that are only adjacent to a single vertex, so this is a slight generalization of the usual definition of a graph. The edges at the boundary of the grid will be called *boundary edges* while the remaining edges will be known as *internal edges*.

For each edge, there is a set of possible labels called *spins*, and a labeling of all the boundary edges will be referred to as a set of *boundary conditions*. A vertex configuration is a choice of spins for the four edges surrounding the vertex. The lattice models we consider assign a so-called *Boltzmann weight* to each vertex configuration which are rational functions, or more precisely elements in the fraction field \mathcal{F} of the complex polynomial ring in some indeterminates associated to lattice model.

We say that a vertex configuration is *admissible* if its Boltzmann weight is non-zero. In this paper we mainly consider lattice models with six types of admissible vertex configurations, which is why they are sometimes called six-vertex models, and the Boltzmann weights for vertices at row i will depend on a row parameter z_i . The rows are numbered $1, \dots, r$ from top to bottom.

A *state* \mathfrak{s} of the model is a labeling of all the edges and we say that the state is *admissible* if every vertex configuration of the state is admissible. Given some specific conditions on the states we define the corresponding *system* \mathfrak{S} of the lattice model to be the set of all states satisfying these conditions. Unless otherwise noted, we will consider systems consisting of all admissible states with some given boundary conditions.

The *partition function* $Z(\mathfrak{S})$ of a system \mathfrak{S} is a weighted sum over the states

$$Z(\mathfrak{S}) := \sum_{\mathfrak{s} \in \mathfrak{S}} \text{wt}(\mathfrak{s}),$$

where the *Boltzmann weight* $\text{wt}(\mathfrak{s})$ of the state \mathfrak{s} is the product of the Boltzmann weights of all its vertices. Note that non-admissible states have vanishing Boltzmann weights, and so even if a system is enlarged to include non-admissible states, the partition function would not be affected.

In this paper, the partition functions will be polynomials in $z_1^{\pm 1}, \dots, z_r^{\pm 1}$ with coefficients depending on, for example, a parameter q . We will consider models whose states can be described by a set of r colored paths going from the top boundary of the grid to either its left or right boundary.

We fix an ordered palette of m colors $\mathcal{P} = \mathcal{P}_m = \{c_1, \dots, c_m\}$ where $c_1 < \dots < c_m$, and will assign a color to each path according to the following rules. The set of possible spins (labellings) of an edge, called a *spin set* is different for horizontal and vertical edges: the possible spins for the horizontal edges are either a color c_1, \dots, c_m or no color at all, while for the vertical edges the possible spins are instead subsets of \mathcal{P} . In other words, there can be at most one path on each horizontal edge, while on the vertical edges the paths can overlap assuming that they have distinct colors. That the vertical edges can only carry at most one path of each color is the reason why the models are called *fermionic* in contrast to *bosonic* models (such as [BN24]) where vertical edges can carry any number of paths for each color. It is not necessary that the number of colors m equals the number of rows r , even though this is often considered for applications in p -adic representation theory such as in [BBBG24a, BBBG21].

The models we will consider are divided into two types: *left-moving* and *right-moving* models. Right-moving models are characterized by the fact that the colored paths start at the top boundary and move down and to the *right* through the grid until they get to the *right* boundary. Left-moving models, on the other hand, are characterized by the fact that the colored paths start at the top boundary and move down and to the *left* through the grid until they get to the *left* boundary. See Figures 2a and 2b for examples of states for these models.



(a) An example state for a right-moving model. (b) An example state for a left-moving model.

Figure 2. Examples of colored states.

For all the models we consider in this paper the admissible vertex configurations have a property we call *color conservation*, which means that if we consider two of the edges of a vertex as *inputs* and the other two as *outputs* then the multiset of input colors is equal to the multiset of output colors. For the left- and right-moving models we assign the input and output edges according to how the paths are allowed to move, i.e. the bottom and right edges are outputs for right-moving models and the bottom and left edges are outputs for the left-moving models, with the remaining edges being inputs.

Because of this color conservation, for an admissible state of the left-moving model the colors of the paths on the left boundary must be a permutation of the colors of the paths on the top boundary, and similarly for the right-moving model. The boundary conditions for a left- or right-moving system can therefore be described by the filled-in columns on the top boundary along with their colors, as well as the permutation of these colors that appear on the left or right boundary, respectively.

2.2. Fusion and boundary conditions. In the previous section we described fermionic models where the vertical edges can carry multiple paths of distinct colors. In order to specify the sets of admissible vertex configurations and their Boltzmann weights we will use an alternative description of these models which is often easier to work with. Instead of using

a subset of the palette \mathcal{P}_m to describe the spin of a vertical edge the alternative description uses a list of m binary elements specifying whether the corresponding colors are included or not. To do this we split each column into m new columns, one for each color of the palette, and restrict each new column to only carry paths of this color (or no path at all). The m new columns corresponding to a single column in the original model will be called a *block*. Due to this expansion of blocks into columns this new description is called the *expanded* model and we will first describe it for the right-moving model, and then see how it relates to the non-expanded version described above. The process is illustrated in Figure 3.

To reiterate, the expanded model has a grid with r rows and Nm columns (m times more than before) and we split the columns into N blocks of m columns. In each block the columns are assigned a column color, from c_1 on the left to c_m on the right. We will also number the columns from *right to left*, starting at 0. Each edge can carry at most one path, and the vertical edges are furthermore limited to paths of the corresponding column color. The admissible vertex configurations are described in Table 1 together with their Boltzmann weights with row parameters z and parameters q and Φ . We also have parameters $\mathfrak{X}_{i,j}$ for $1 \leq i, j \leq r$ which satisfy

$$(2.1) \quad \begin{cases} \mathfrak{X}_{i,i} = -q^2 \\ \mathfrak{X}_{i,j}\mathfrak{X}_{j,i} = q^2 \text{ for } i \neq j. \end{cases}$$

The Boltzmann weights are thus viewed as elements of the fraction field $\mathcal{F} = \mathbb{C}(q, z_i, \Phi, \mathfrak{X}_{i,j})$ for all i and j where $j > i$.

We will now describe how the boundary conditions for the expanded model is given by a list of colors $\sigma = (\sigma_1, \dots, \sigma_r) \in \mathcal{P}^r$ and a list of column numbers $\mu = (\mu_1, \dots, \mu_r) \in (\mathbb{Z}_{\geq 0})^r$ with $\mu_1 > \mu_2 > \dots > \mu_r$. Here we assume that $Nm \geq \mu_1$, which we can make sure is true by choosing N to be sufficiently large. Firstly, there are no paths on the left and bottom boundaries. Secondly, for the top boundary there is a path on the edges with column numbers μ_1, \dots, μ_r of the corresponding column color (remember that vertical edges are only allowed to carry a path of a specific color), which explains why the assumption $Nm \geq \mu_1$ is required. Finally, for the right boundary there is a path on every edge, and the color of the path on the i^{th} row is σ_i indexed, as before, from the top down. Because of color conservation for admissible states, σ needs to be a permutation of the top boundary colors.

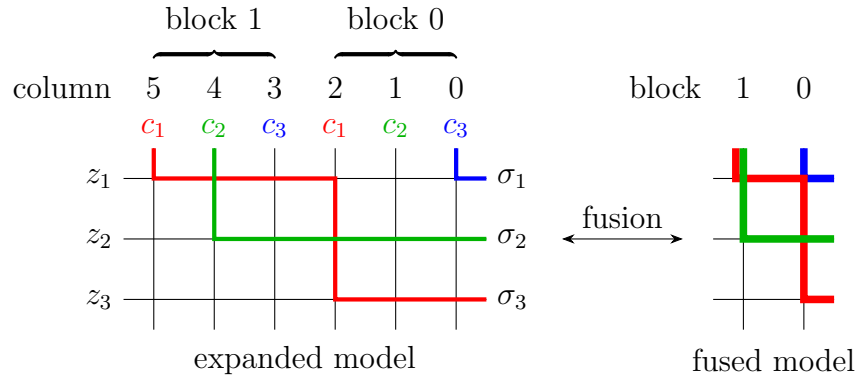


Figure 3. A state for the unfused right-moving model with boundary data given by $\mu = (5, 4, 0)$ and $\sigma = (c_3, c_2, c_1)$ and its corresponding fused description.

Table 1. The vertex configurations T_R for the family of right-moving models considered in this paper together with the corresponding Boltzmann weights. Here, c_j is the column color and c_i is the color of a path.

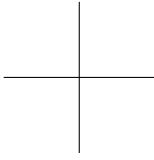
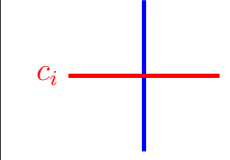
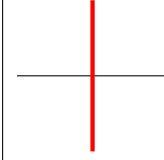
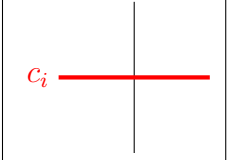
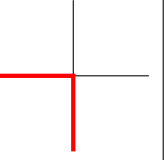
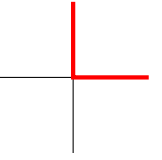
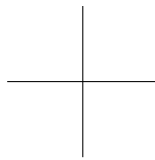
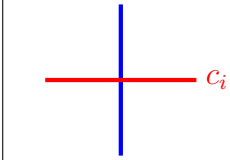
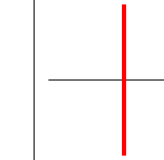
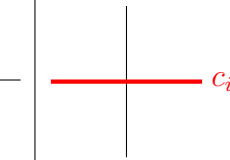
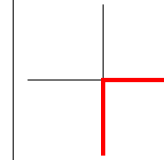
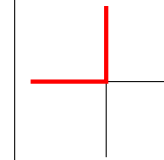
T_R					
a_1	a_2	b_1	b_2	c_1	c_2
c_j 	c_j 	c_j 	c_j 	c_j 	c_j 
1	$\Phi \mathfrak{X}_{i,j} \begin{cases} z & i = j \\ 1 & i \neq j \end{cases}$	Φ	$\begin{cases} z & i = j \\ 1 & i \neq j \end{cases}$	$\Phi(1 - q^2)z$	1

Table 2. The vertex configurations T_L for the family of left-moving models considered in this paper together with the corresponding Boltzmann weights. Here, c_j is the column color and c_i is the color of a path.

T_L					
a_1	a_2	b_1	b_2	c_1	c_2
c_j 	c_j 	c_j 	c_j 	c_j 	c_j 
1	$\Phi \mathfrak{X}_{j,i} \begin{cases} z^{-1} & i = j \\ 1 & i \neq j \end{cases}$	Φ	$\begin{cases} z^{-1} & i = j \\ 1 & i \neq j \end{cases}$	$\Phi(1 - q^2)$	z^{-1}

See Figure 3 for an example of a state for this model. Note that the partition function does not depend on N as long as $Nm \geq \mu_1$, because every vertex to the left of column μ_1 will be an a_1 vertex, which has Boltzmann weight 1. We will denote by $\mathfrak{S}_{\mu,\sigma}^R$ the system with these boundary conditions and usually abbreviate the partition function $Z(\mathfrak{S}_{\mu,\sigma}^R)(\mathbf{z})$ to $Z_{\mu,\sigma}^R(\mathbf{z})$, where $\mathbf{z} = (z_1, z_2, \dots, z_r)$.

The process of going from this expanded model to the one we started with by merging the single-colored columns in a block into a single column is known as *fusion*, and therefore we will call the models introduced in Section 2.1 *fused*. We will similarly sometimes call the expanded models *unfused*. Given an expanded model, we can find the admissible vertex configurations and the Boltzmann weights of the corresponding fused model by considering a one-row one-block grid, which corresponds to a single vertex in the fused model. Any given vertex configuration for the fused model gives us boundary conditions of the expanded

one-row one-block grid, i.e. in the following equality we are given the fused edge spins A , B , C and D , which determine the expanded edge spins as A , B_i , C and D_i by setting B_i to carry a path if there is a path of color c_i in B and similarly for D_i and D .

Given boundary conditions of the expanded one-row one-block grid, there is at most one way to color the internal edges because of color conservation. If there is an admissible expanded state then we say that the fused vertex configuration we started with was admissible, and its weight is equal to that of the expanded state, i.e. the product of the weights of the m expanded vertices.

$$\text{wt} \left(\begin{array}{c} (B) \\ | \\ (A) \text{---} (C) \\ | \\ (D) \end{array} \right) = \text{wt} \left(\begin{array}{ccccccc} & c_1 & c_2 & c_3 & & c_m & \\ & (B_1) & (B_2) & (B_3) & & (B_m) & \\ & | & | & | & & | & \\ (A) & \text{---} & & & \cdots & & \text{---} & (C) \\ & | & | & | & & | & \\ & (D_1) & (D_2) & (D_3) & & (D_m) & \end{array} \right)$$

If there is no admissible expanded state, then the fused vertex configuration was not admissible and the Boltzmann weight is set to zero.

The expanded description of the left-moving model is similarly defined and the fusion process is the same. Specifically, the spin sets are the same as for the expanded Delta model and the m column colors of the expanded columns in a block are still c_1, \dots, c_m from left to right. The admissible vertex configurations and their Boltzmann weights are listed in Table 2. The boundary conditions for the top boundary are determined by μ in the same way as for the right-moving model, and the left boundary colors are given by σ in the same way as the right boundary colors for the right-moving model.

It is not difficult to see that with these boundary conditions, \mathbf{b}_2 is the only vertex configuration that can appear to the left of column μ_1 . Since the Boltzmann weight of the \mathbf{b}_2 vertex configuration in Table 2 is not identically 1, the partition function of the left-moving model actually depends on the number of blocks N , in contrast to the right-moving model. We will therefore denote by $\mathfrak{S}_{\mu,\sigma}^{\mathbf{L},N}$ the system with the boundary conditions above, and by $\mathfrak{S}_{\mu}^{\mathbf{L},N}$ the system where we drop the condition on the colors on the left-hand side. Furthermore, we will usually abbreviate the partition functions $Z(\mathfrak{S}_{\mu,\sigma}^{\mathbf{L},N})(\mathbf{z})$ and $Z(\mathfrak{S}_{\mu}^{\mathbf{L},N})(\mathbf{z})$ to $Z_{\mu,\sigma}^{\mathbf{L},N}(\mathbf{z})$ and $Z_{\mu}^{\mathbf{L},N}(\mathbf{z})$, respectively. In both of these cases, if N is increased by 1, then the partition function is multiplied by $\mathbf{z}^{(1,\dots,1)} = z_1 z_2 \cdots z_r$.

2.3. Specializations. We are interested in two specializations of these models which are related to two different types of Whittaker functions, namely metaplectic (spherical) Whittaker functions and (non-metaplectic) Iwahori Whittaker functions. The two specializations are:

$$(2.2) \quad \textbf{Metaplectic specialization:} \quad \Phi = 1 \quad \mathfrak{X}_{i,j} = g(j-i) \quad q^2 = v$$

$$(2.3) \quad \textbf{Iwahori specialization:} \quad \Phi = -v \quad \mathfrak{X}_{i,j} = \begin{cases} -1 & i < j \\ -1/v & i \geq j \end{cases} \quad q^2 = 1/v.$$

Here, the reparametrization of q in terms of v is due to historical reasons, and $g(a)$ is a Gauss sum which is a particular sum over roots of unity ubiquitous in number theory and which satisfies (2.1). We will call the corresponding lattice models left- and right-moving metaplectic ice and Iwahori ice, respectively, and their weights are shown in Tables 3 and 4.

Let us now describe how these specializations relate to existing lattice models in the literature. See also Figure 1.

- The right-moving Iwahori ice model is exactly the one defined in [BBBG24a] for computing values of Iwahori Whittaker functions of unramified principal series of $\mathrm{GL}_r(F)$ where F is a non-archimedean field with residue field cardinality $1/v$.
- The left-moving Iwahori ice model is new and the construction of this model was a motivation for this paper. The reason for this will be explained in the next paragraph.
- The right-moving metaplectic ice model is equivalent to the metaplectic Δ' -model of [BBBG24b] by a reparametrization of row parameters and an exchange of colors with supercolors (as explained therein). The Δ' -model is in turn related to the Δ -model of the same paper by a change of basis for the spin sets.
- The left-moving metaplectic ice model is equivalent to the metaplectic Γ -model of [BBBG24b] after reparametrizing the row parameters, multiplying the T -weights by z , applying the same change of basis and exchanging colors with supercolors as above.

The Δ and Γ metaplectic models actually give the same partition functions (up to reversing \mathbf{z}) and were originally defined in [BBB19, BBC⁺12] to compute values of metaplectic spherical Whittaker functions. The fact that the Γ and Δ variants give the same partition functions is non-trivial and was proven in an intricate combinatorial argument in [BBF11b] and later using Yang–Baxter equations in [BBB19, BBBG17]. The identity, which is called the Γ - Δ duality, is not a state-by-state identity but requires a complicated interplay between the terms of the partition function coming from differently sized sets of states on the two sides. The duality was used in [BBBG24b] to prove an unexpected and surprising equality of non-metaplectic Iwahori Whittaker functions and metaplectic spherical Whittaker functions.

One important goal of this paper was to construct a dual, left-moving model to the existing right-moving Iwahori model mirroring the above story for the metaplectic specialization. In Section 3.3 we will actually show that the whole left- and right-moving families described in this section are dual to each other, giving the same partition functions as detailed in Theorem 3.10.

Remark 2.1. Since the metaplectic specialization of the left-moving model is called a Γ model and the right-moving model a Δ model, it may be tempting to classify the whole left- and right-moving family as Γ and Δ models, respectively. Indeed, we used this terminology in early talks about this work. However, we thank Daniel Bump for pointing out to us that the right-moving Iwahori ice model reduces to a Γ model when the palette size $m = 1$. This corresponds to a non-metaplectic spherical Whittaker function (and is thus a common point of origin for Iwahori ice and metaplectic ice). Thus, the right-moving Iwahori ice model should instead be classified as a Γ model instead of a Δ model for all m . Its left-moving dual reduces to a Δ model for $m = 1$ and will therefore be called a Δ model for all m . See Figure 1. As we will see in the next subsection this naming convention for the Iwahori specialization also agrees with the models in the $v \rightarrow 0$ limit studied in [BS22].

Since the Γ - Δ classification is therefore not an invariant for the continuous families of lattice models we will in this paper mostly use the terminology left- and right-moving and will use the terminology Γ and Δ only for the Iwahori or the metaplectic specializations.

In the next subsection we discuss the $v \rightarrow 0$ limit of the Iwahori ice models where the left-right duality does reduce to a state-by-state equality.

2.4. Crystal models. In the Iwahori specialization of both the left-moving and right-moving families we will now consider the limit $v \rightarrow 0$, known as the *crystal limit* since it is connected to crystal bases of the quantum group defined by [Kas90, Lus90]. For convenience the weights can be found in Tables 3 and 4. Note that in the crystal limit the \mathbf{b}_1 weight becomes zero and thus the \mathbf{b}_1 vertex configuration is no longer admissible. For the \mathbf{a}_2 configuration the weight also vanishes in the case $i < j$, which means that paths of distinct colors are only allowed to cross in one direction, and then those two paths cannot cross again.

Lemma 2.2. *Suppose we have an admissible vertex configuration of the crystal limit $v \rightarrow 0$ of the Iwahori specialization of the fused left- or right-moving model (i.e. Δ and Γ , respectively). If the bottom edge carries at most one colored path, then the same is true for the top edge.*

Proof. We will start with the right-moving case. Recall that by color conservation, the multiset of colors on the bottom and right edges is the same as the multiset of colors on the top and left edges. Since the horizontal edges can carry at most one color, this means that the top edge can carry at most one color more than the bottom edge.

The statement then immediately holds in the case where the bottom edge has no colors at all. So suppose that the bottom edge has a single color C , and furthermore that the top edge carries two colors D and E which must therefore be distinct because the vertical edges are fermionic. If neither D nor E is equal to C , then we would get a contradiction from color conservation and the fact that the horizontal edges carry at most a single color. So we may assume that $E = C$.

Recall that the column colors are increasing from left to right. If $D < C$ then we have the following situation

$$(2.4) \quad \begin{array}{c} DC \\ \text{---} \text{---} \\ | \\ \text{---} \end{array}$$

which has weight 0 according to the first case of the \mathbf{a}_2 weight in Table 3. On the other hand, if $C < D$ we have

$$(2.5) \quad \begin{array}{c} CD \\ | \\ \text{---} \end{array}$$

which has weight 0 according to the \mathbf{b}_1 weight. So in both cases we reach a contradiction. Thus we have shown that the top edge can carry at most one color which finishes the proof for the right-moving case.

The proof for the left-moving case is analogous. □

Recall that in our usual boundary conditions for a system the edges along the bottom boundary carry no paths; in other words they are unoccupied. By arguing inductively upwards from the bottom row the above lemma then implies that the only vertex configurations that can appear in an admissible state are those with at most one color on the vertical paths. Since we are always going to impose boundary conditions of this kind, we can restrict the crystal models to these admissible vertex configurations without affecting the partition functions, and from now on, it is always this restricted set of admissible vertex configurations that we will use for crystal models.

Table 3. Specializations of the unfused right-moving model T_R .

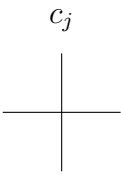
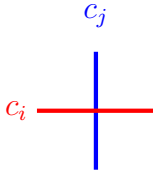
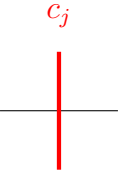
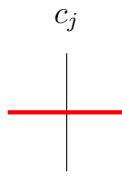
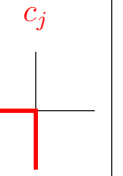

T_R (specializations, unfused)						
	a_1	a_2	b_1	b_2	c_1	c_2
						
Metaplectic Δ	1	$g(j-i) \begin{Bmatrix} z & i=j \\ 1 & i \neq j \end{Bmatrix}$	1	$\begin{Bmatrix} z & i=j \\ 1 & i \neq j \end{Bmatrix}$	$(1-v)z$	1
Iwahori Γ	1	$\begin{Bmatrix} v & i < j \\ z & i=j \\ 1 & i > j \end{Bmatrix}$	$-v$	$\begin{Bmatrix} z & i=j \\ 1 & i \neq j \end{Bmatrix}$	$(1-v)z$	1
Crystal Γ	1	$\begin{Bmatrix} 0 & i < j \\ z & i=j \\ 1 & i > j \end{Bmatrix}$	0	$\begin{Bmatrix} z & i=j \\ 1 & i \neq j \end{Bmatrix}$	z	1

Table 4. Specializations of the unfused left-moving model T_L .

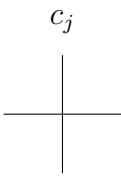
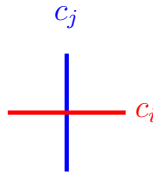
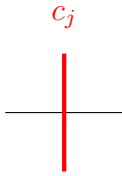
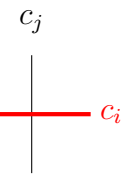
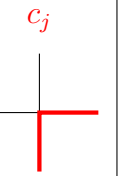

T_L (specializations, unfused)						
	a_1	a_2	b_1	b_2	c_1	c_2
						
Metaplectic Γ	1	$g(i-j) \begin{Bmatrix} z^{-1} & i=j \\ 1 & i \neq j \end{Bmatrix}$	1	$\begin{Bmatrix} z^{-1} & i=j \\ 1 & i \neq j \end{Bmatrix}$	$1-v$	z^{-1}
Iwahori Δ	1	$\begin{Bmatrix} 1 & i < j \\ z^{-1} & i=j \\ v & i > j \end{Bmatrix}$	$-v$	$\begin{Bmatrix} z^{-1} & i=j \\ 1 & i \neq j \end{Bmatrix}$	$1-v$	z^{-1}
Crystal Δ	1	$\begin{Bmatrix} 1 & i < j \\ z^{-1} & i=j \\ 0 & i > j \end{Bmatrix}$	0	$\begin{Bmatrix} z^{-1} & i=j \\ 1 & i \neq j \end{Bmatrix}$	1	z^{-1}

Table 5. The vertex configurations and weights of the fused Gamma Iwahori crystal model with at most one color on the vertical edges.

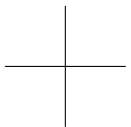
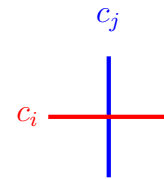
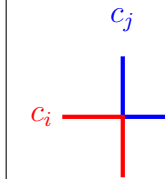
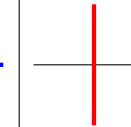
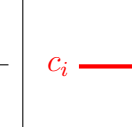
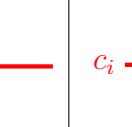
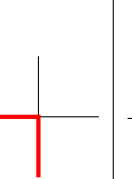
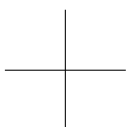
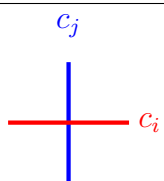
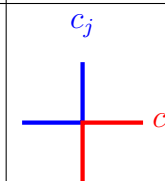
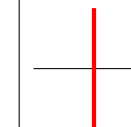

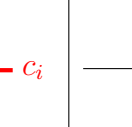
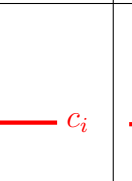
$\mathbf{T_R = T_\Gamma}$ (fused crystal limit)						
$\mathbf{a_1}$	$\mathbf{a_2}$	$\mathbf{a'_2}$	$\mathbf{b_1}$	$\mathbf{b_2}$	$\mathbf{c_1}$	$\mathbf{c_2}$
						
1	$\begin{cases} 0 & i < j \\ z & i \geq j \end{cases}$	$\begin{cases} z & i < j \\ 0 & i > j \end{cases}$	0	z	z	1

Table 6. The vertex configurations and weights obtained by fusing the Delta Iwahori crystal model, restricting to at most one color on the vertical edges and then multiplying each weight by z . The multiplication by z is convenient since it removes the dependence on the number of columns for the partition function.

$\mathbf{zT_L = zT_\Delta}$ (fused crystal limit)						
$\mathbf{a_1}$	$\mathbf{a_2}$	$\mathbf{a'_2}$	$\mathbf{b_1}$	$\mathbf{b_2}$	$\mathbf{c_1}$	$\mathbf{c_2}$
						
z	$\begin{cases} 1 & i \leq j \\ 0 & i > j \end{cases}$	$\begin{cases} 0 & i < j \\ 1 & i > j \end{cases}$	0	1	z	1

Following Section 2.2, we can compute the Boltzmann weights of the fused admissible vertex configurations with at most one color on the vertical paths, and these can be found in Tables 5 and 6. The weights of the latter have been multiplied by z which conveniently removes the partition function's dependence on the number of columns, since any extra $\mathbf{b_2}$ configurations added on the left side of the grid would only contribute by a factor of 1. We make this change *after* the fusion process instead of making an analogous change for the unfused weights for the whole family to avoid factors of $z^{1/m}$.

As an example, Figure 4 illustrates the weight computation for one case of the $\mathbf{a'_2}$ vertex configuration.

3. SOLVABILITY AND YANG–BAXTER EQUATIONS

In this section we will show that the families of left- and right-moving models introduced in Section 2 satisfy various Yang–Baxter equations. The general Yang–Baxter equation with respect to three vector spaces (or quantum group modules) U , V and W as well as three

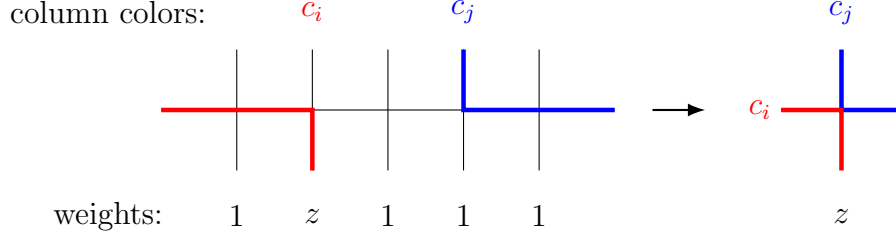


Figure 4. Fusion of an \mathbf{a}'_2 vertex of the left-moving Iwahori crystal model with $i < j$.

linear maps $R : U \otimes V \rightarrow V \otimes U$, $S : U \otimes W \rightarrow W \otimes U$ and $T : V \otimes W \rightarrow W \otimes V$ is the following functional equation

$$(3.1) \quad \llbracket R, S, T \rrbracket := (\mathbb{1}_W \otimes R)(S \otimes \mathbb{1}_V)(\mathbb{1}_U \otimes T) - (T \otimes \mathbb{1}_U)(\mathbb{1}_V \otimes S)(R \otimes \mathbb{1}_W) = 0$$

as maps $U \otimes V \otimes W \rightarrow W \otimes V \otimes U$. This definition of the Yang–Baxter commutator $\llbracket R, S, T \rrbracket$ is related the one used in, for example, [BBF11a] which considers endomorphisms of $U \otimes V$ instead of maps $U \otimes V \rightarrow V \otimes U$. They are related by applications of the linear map τ defined on pure tensors by $a \otimes b \mapsto b \otimes a$.

In the lattice model, the spaces U , V and W have bases enumerated by the spin sets of either vertical edges, or horizontal edges of left-moving type (L) or right-moving type (R) corresponding to the type of the model. The horizontal vector spaces, and their associated maps, depend on parameters z_i for row i and we will denote them by $V_L(z_i)$ and $V_R(z_i)$.

We will consider two cases. In the first case, called the *RTT*-equation, W corresponds to vertical edges, and $U = V_X(z_1)$ and $V = V_Y(z_2)$ are horizontal edges of type X and Y (with $X, Y \in \{\text{L}, \text{R}\}$). This means that $S : V_X(z_1) \otimes W \rightarrow W \otimes V_X(z_1)$ and $T : V_Y(z_2) \otimes W \rightarrow W \otimes V_Y(z_2)$ are maps involving both horizontal and vertical edges and we will associate them with the standard vertices \uparrow in the lattice model, which we will call *T*-vertices and we write $S = T_X$ and $T = T_Y$. The map $R := R_{XY} : V_X(z_1) \otimes V_Y(z_2) \rightarrow V_Y(z_2) \otimes V_X(z_1)$ involves only horizontal edges for two different rows and can be seen as swapping these rows. In the lattice model we associate this map with a new type of vertex \times connecting four horizontal edges.

The lattice model description of (3.1) in the *RTT*-case states that the partition functions for the following systems with fixed boundary conditions are equal.

$$(3.2) \quad \llbracket R_{XY}, T_X, T_Y \rrbracket = 0 :$$

The internal edges i , j , k , l , m and n are summed over while the boundary edges are kept fixed. These *RTT*-equations can be used to obtain functional equations for partition functions

by a repeated use of (3.2) in what is called the *train argument*, see for example the proof of Lemma 3.11.

The other type of Yang–Baxter equation we will consider consists of three R -vertices and is therefore called the RRR -equation. Here $U = V_X(z_1)$, $V = V_Y(z_2)$ and $W = V_Z(z_3)$ all correspond to horizontal edges of row types $X, Y, Z \in \{L, R\}$ with different row parameters z_1, z_2 and z_3 . The lattice model description of (3.1) for the RRR -equation states that the partition functions for the following systems with fixed boundary conditions are equal.

$$(3.3) \quad \llbracket R_{XY}, R_{XZ}, R_{YZ} \rrbracket = 0:$$

As before, the internal edges i, j, k, l, m and n are summed over while the boundary edges are kept fixed. Note how this picture is just a slight rearrangement of the one in (3.2).

We say that a (fused) lattice model is *solvable* if all of the above Yang–Baxter equations hold. The fusion process described in Section 2.2 for constructing lattice models was developed in [BBBG24a] and Lemma 5.4 therein shows that if the unfused model satisfies *auxiliary* or *unfused* Yang–Baxter equations then this implies that the fused models satisfy the standard Yang–Baxter equations. These auxiliary Yang–Baxter equations are very similar to those in (3.2) and (3.3) except the vertices now carry a vertex color, all being the same color c_k for some k except for the R -vertex in the right-hand side of (3.2) which is c_{k+1} (where $c_{m+1} = c_1$). The fused R -vertex is obtained by restricting to $k = 1$. Since the auxiliary Yang–Baxter equations imply the standard Yang–Baxter equations we will often drop the term *auxiliary* even for unfused models.

We present the different (unfused) R -vertices and their weights for our models in Tables 7 and 8 and the following theorem states that they, together with the different T -vertices presented before satisfy all the Yang–Baxter equations of (3.2) and (3.3).

Theorem 3.1. *The unfused R -vertices of Tables 7 and 8 and T -vertices of Tables 1 and 2 satisfy the auxiliary Yang–Baxter RTT -equations in (3.2) and the RRR -equations in (3.3) for all combinations of row types $X, Y, Z \in \{L, R\}$.*

It follows from Lemma 5.4 in [BBBG24a] that the fused models satisfies the standard Yang–Baxter equations in (3.2) and (3.3) for all $X, Y, Z \in \{L, R\}$.

Corollary 3.2. *The fused left- and right-moving models are solvable.*

We will prove Theorem 3.1 by showing that the Yang–Baxter equations are satisfied for a specific choice of Φ and $\mathfrak{X}_{i,j}$, and that this then implies that they hold for all Φ and $\mathfrak{X}_{i,j}$.

For this choice it would be possible to choose the metaplectic specialization where many of the Yang–Baxter equations are proven. For example all the metaplectic RTT -equations are shown in [BBB19, Gra17] and the metaplectic $X = Y = Z = \Gamma$ RRR -equation in

Table 7. Configurations and Boltzmann weights for the expanded, unfused R_L^L and R_R^R attaching to the left of two vertically aligned T -vertices with vertex color c_k and row parameters z_1 above z_2 . The row parameters are swapped by the R -vertices so that z_2 is above z_1 at the R -vertices' left edges as shown in the first column. Here $i \neq j$ and the weights on the first row are equal for R_L^L and R_R^R after substituting Φ with $1/(q^2\Phi)$, thus exchanging the second and third weights, while for the second row they are equal after swapping z_1 and z_2 .

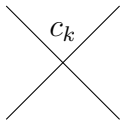
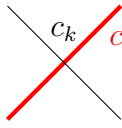
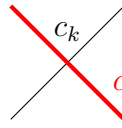
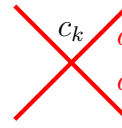
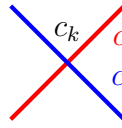
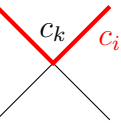
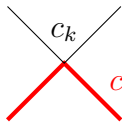
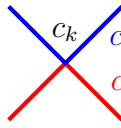
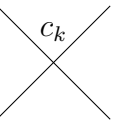
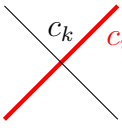
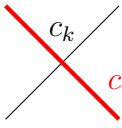
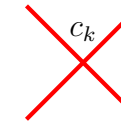
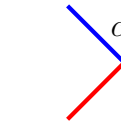
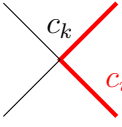
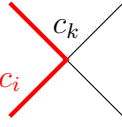
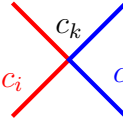
R_L^L and R_R^R					
z_2					
z_1					
R_L^L	$z_1 - q^2 z_2$	$q^2 \Phi(z_1 - z_2)$	$(z_1 - z_2)/\Phi$	$z_2 - q^2 z_1$	$\mathfrak{X}_{i,j}(z_1 - z_2)$
R_R^R	$\Phi \longrightarrow 1/(q^2 \Phi)$				
z_2					
z_1					
R_L^L	$(1 - q^2)z_1$	$(1 - q^2)z_2$	$(1 - q^2) \cdot \begin{cases} z_2 & \text{if } i < j < k \text{ or } j < k \leq i \text{ or } k \leq i < j \\ z_1 & \text{if } j < i < k \text{ or } i < k \leq j \text{ or } k \leq j < i \end{cases}$		
R_R^R	$z_1 \longleftrightarrow z_2$				

Table 8. Configurations and Boltzmann weights for the expanded, unfused R_R^L and R_L^R attaching to the left of two vertically aligned T -vertices with vertex color c_k and row parameters z_1 above z_2 . The row parameters are swapped by the R -vertices so that z_2 is above z_1 at the R -vertices' left edges as shown in the first column. Here $i \neq j$ and the conditions for the last weights are the same as in Table 4.

R_R^L and R_L^R					
z_2					
z_1					
R_R^L	$z_1 - z_2$	$\Phi(z_1 - q^2 z_2)$	$\Phi(z_1 - q^2 z_2)$	$\Phi^2(q^4 z_2 - z_1)$	$\Phi^2 \mathfrak{X}_{j,i}(z_1 - q^2 z_2)$
R_L^R	$z_2 - q^{2m+2} z_1$	$(z_2 - q^{2m} z_1)/\Phi$	$(z_2 - q^{2m} z_1)/\Phi$	$(q^{2m-2} z_1 - z_2)/\Phi^2$	$\frac{\mathfrak{X}_{j,i}}{(q\Phi)^2}(z_2 - q^{2m} z_1)$
z_2					
z_1					
R_R^L	$\Phi(1 - q^2)z_1$	$\Phi(1 - q^2)z_2$	$-\Phi^2(1 - q^2) \cdot \begin{cases} q^2 z_2 & \text{if } i < j < k, \dots \\ z_1 & \text{if } j < i < k, \dots \end{cases}$		
R_L^R	$\frac{q^{2 \text{res}_m(k-i)-2}}{\Phi}(1 - q^2)z_2$	$\frac{q^{2 \text{res}_m(i-k)}}{\Phi}(1 - q^2)z_1$	$\frac{q^{2 \text{res}_m(i-j)-2}}{\Phi^2}(1 - q^2) \cdot \begin{cases} z_1 & \text{if } i < j < k, \dots \\ z_2 & \text{if } j < i < k, \dots \end{cases}$		

[BBB19]. The remaining metaplectic equations should be able to be obtained from the preprint [BBBG17]. However, the relevant part of the preprint was not included in the published version which appeared as an appendix to [BBB19] and it relied itself on results in the preprint of [BBB19] which were also not published.

In what follows we will instead give an independent and self-contained proof of Theorem 3.1 starting from the Iwahori specialization where many things simplify drastically. The Yang–Baxter equations involving only right-moving row types were originally proved in [BBBG24a], but we do not rely on this proof either since this case is covered by our general argument with no additional effort. We choose this particular specialization because all the Iwahori T -weights in Tables 3 and 4 and the Iwahori specializations of the R -weights in Tables 7 and 8 except for R_L^R depend on the color indices i, j , and k only by their relative orders in the palette. In contrast, R_L^R depends on the actual values of i, j , and k for the involved colors. Indeed, R_L^R depends on the residues

$$[0, m-1] \ni \text{res}_m(x) \equiv x \equiv \text{res}^m(x) \in [1, m].$$

This is important since we want to reduce the proof of the Yang–Baxter equation to checking a finite number of equations independent of m .

We do not actually need the Yang–Baxter equations involving R_L^R for the rest of this paper, but we will, for completeness, show that the Yang–Baxter equations involving R_L^R follow from the other equations appearing in Theorem 3.1 using the following lemma and proposition.

Lemma 3.3. *If $R_{XY}R_{YX} = \mathbb{1}_{V_X} \otimes \mathbb{1}_{V_Y}$ and $R_{YX}R_{XY} = \mathbb{1}_{V_Y} \otimes \mathbb{1}_{V_X}$ then*

$$(3.4) \quad \llbracket R_{XY}, T_X, T_Y \rrbracket = 0 \iff \llbracket R_{YX}, T_Y, T_X \rrbracket = 0$$

and

$$(3.5) \quad \llbracket R_{XY}, R_{XY}, R_{YY} \rrbracket = 0 \iff \llbracket R_{YX}, R_{YY}, R_{XY} \rrbracket = 0 \iff \llbracket R_{YY}, R_{YX}, R_{YX} \rrbracket = 0$$

Proof. From the definition (3.1) for the Yang–Baxter bracket we get by direct computation that

$$\begin{aligned} (\mathbb{1} \otimes R_{YX}) \llbracket R_{XY}, T_X, T_Y \rrbracket (R_{YX} \otimes \mathbb{1}) &= -\llbracket R_{YX}, T_Y, T_X \rrbracket \\ (\mathbb{1} \otimes R_{YX}) \llbracket R_{XY}, R_{XY}, R_{YY} \rrbracket (R_{YX} \otimes \mathbb{1}) &= -\llbracket R_{YX}, R_{YY}, R_{XY} \rrbracket \\ (R_{YX} \otimes \mathbb{1}) \llbracket R_{YX}, R_{YY}, R_{XY} \rrbracket (\mathbb{1} \otimes R_{YX}) &= -\llbracket R_{YY}, R_{YX}, R_{YX} \rrbracket. \end{aligned} \quad \square$$

See also [Nap22, Lemma 4.1 and Corollary 4.2] for similar results in another setting.

Proposition 3.4. *The maps R_R^L and R_L^R for the lattice models of this paper defined by Table 8 satisfy*

$$R_R^L(z_2, z_1)R_L^R(z_1, z_2) = C \cdot \mathbb{1}_{V_R} \otimes \mathbb{1}_{V_L} \quad \text{and} \quad R_L^R(z_1, z_2)R_R^L(z_2, z_1) = C \cdot \mathbb{1}_{V_L} \otimes \mathbb{1}_{V_R}$$

where $C = (z_2 - q^2 z_1)(z_2 - q^{2m} z_1)$.

See Appendix A for the proof. Diagrammatically the first equation corresponds to showing that

$$(3.6) \quad \begin{array}{c} R_R^L \quad R_L^R \\ \begin{array}{ccc} b & & c \\ & \diagdown \quad \diagup & \\ a & \bullet & \bullet \\ & \diagup \quad \diagdown & \\ & & d \end{array} \end{array} = \begin{array}{ccc} b & \text{-----} & c \\ a & \text{-----} & d \end{array}$$

In contrast to the other proofs of this section, the computations in Appendix A depend strongly on the number of colors m especially since the interior edges on the left-hand side of (3.6) can become a sum over all m colors of the palette even for fixed, given boundary edges a, b, c and d . Similar *color loops* can occur in Yang–Baxter equations involving R_L^R , and it is somewhat surprising that we obtain such a simple right hand side in Proposition 3.4, and that the Yang–Baxter equations hold for all m . As we show in Appendix A, this is explained by the fact that these sums of internal color loops become telescoping sums resulting in this simple expression for C .

Since we may rescale R_L^R by C without affecting the Yang–Baxter equation we reach the following conclusion from combining Lemma 3.3 and Proposition 3.4.

Corollary 3.5. *To prove Theorem 3.1 it is enough to prove the cases which do not involve R_L^R (i.e. those involving only T_R, T_L, R_R^R, R_L^L and R_R^L).*

Lemma 3.6. *For fixed boundary conditions, the admissible states in a Yang–Baxter equation without vertices of type R_L^R (i.e. consisting only of types T_R, T_L, R_R^R, R_L^L and R_R^L) involve at most three colors, and those must appear on the boundary and therefore be fixed.*

Proof. As a first step, we would like to show that in an admissible state of either of the systems in (3.2) and (3.3), any color appearing on an internal edge must also appear on the boundary. From this it would follow that when we compute the partition functions, we only need to consider the colors that appear on the boundary.

To show this, first consider the system on the left-hand side of the RTT -equation in (3.2) and suppose, for a contradiction, that we have an admissible state with an internal edge with a color that does not appear on the boundary. Because of color conservation, this is only possible if $R_{XY} = R_R^L, T_X = T_R$ and $T_Y = T_L$, but that is not a compatible choice of R - and T -vertices. Similarly, for the right-hand side of (3.2) we could argue that we must have $R_{XY} = R_R^L, T_X = T_R$ and $T_Y = T_L$, which again is not a compatible choice of R - and T -vertices.

For the left-hand side of the RRR -equation in (3.3) we would be forced to have $R_{XY} = R_R^L$ and $R_{YZ} = R_R^L$ and hence $R = Y = L$, a contradiction. Similarly, for the right-hand side we would be forced to have $R_{YZ} = R_R^L$ and $R_{XY} = R_R^L$ and hence $L = Y = R$, a contradiction.

Thus we have showed that any color appearing on an internal edge of an admissible state must also appear on the boundary, and it only remains to be shown that an admissible state can have at most three colors on the boundary. So consider some colored edge on the boundary of an admissible state. By color conservation, it is part of a path of this color through the system and since one end of the path is on the boundary, the other one must also be on the boundary. Hence any color on the boundary must appear at least twice on the boundary, which means that there can be at most three distinct colors on the six boundary edges.

So the boundary conditions can involve at most three distinct colors which are fixed for the whole system, and any admissible state can only involve those three colors. \square

Proposition 3.7. *If Theorem 3.1 holds for a particular choice of $\Phi \neq 0$ and $\mathfrak{X}_{i,j}$ satisfying (2.1), then it holds for all such Φ and $\mathfrak{X}_{i,j}$.*

Proof. The proof generalizes those of Propositions 4.12 and 4.14 of [BBBG24b] where all involved vertices are right-moving. We will show that for fixed boundary edges, all state

Table 9. The factors of Φ and ϕ appearing in the weights of Tables 1, 2, 7 and 8. The arrows signify our choices of inputs and outputs such that colors are conserved.

Vertex type	Input \rightarrow Output	ϕ -factor	Φ -factor
$\begin{array}{c} b \\ \\ a - \text{---} c \\ \\ d \end{array}$	$T_R \quad \searrow$	$\exp\left(\frac{1}{4}\langle a+c, b+d \rangle\right)$	$\Phi^{\langle d \rangle}$
	$T_L \quad \swarrow$	$\exp\left(-\frac{1}{4}\langle a+c, b+d \rangle\right)$	$\Phi^{\langle d \rangle}$
$\begin{array}{c} b \quad c \\ \diagdown \quad \diagup \\ a \quad d \end{array}$	$R_R^R \quad \rightarrow$	$\exp\left(\frac{1}{4}\langle a+c, b+d \rangle\right)$	$\Phi^{\frac{\langle -a-c+b+d \rangle}{2}}$
	$R_L^L \quad \leftarrow$	$\exp\left(\frac{1}{4}\langle a+c, b+d \rangle\right)$	$\Phi^{\frac{\langle a+c-b-d \rangle}{2}}$
	$R_R^L \quad \downarrow$	$\exp\left(-\frac{1}{4}\langle a+c, b+d \rangle\right)$	$\Phi^{\frac{\langle a+c+b+d \rangle}{2}}$
	$R_L^R \quad \uparrow$	$\exp\left(-\frac{1}{4}\langle a+c, b+d \rangle\right)$	$\Phi^{\frac{\langle -a-c-b-d \rangle}{2}}$

configurations appearing on either side of the Yang–Baxter equations (either RTT or RRR) have the same factors of Φ and $\mathfrak{X}_{i,j}$.

For these manipulations it is convenient to interpret the unfused edge spins as maps $\mathcal{P} \rightarrow \{0, 1\}$, where $\mathcal{P} = \mathcal{P}_m$ is the palette, and lift these to the ring \mathcal{P}^* of maps $\mathcal{P} \rightarrow \mathbb{Z}$. For $f \in \mathcal{P}^*$ we define the \mathcal{P} -average $\langle f \rangle = \sum_{c \in \mathcal{P}} f(c) \in \mathbb{Z}$ which is linear in f .

We also let $\phi : \mathcal{P} \times \mathcal{P} \rightarrow \mathbb{C}^\times$ such that

$$(3.7) \quad \phi(c, d)\phi(d, c) = 1 \text{ and } \phi(c, c) = 1 \text{ for all } c, d \in \mathcal{P}$$

and introduce the antisymmetric bilinear form $\langle, \rangle : \mathcal{P}^* \times \mathcal{P}^* \rightarrow \mathbb{C}$ defined by

$$\langle f, g \rangle = \sum_{c, d \in \mathcal{P}} f(c)g(d) \log \phi(c, d)$$

for $f, g \in \mathcal{P}^*$. Here we chosen have a branch cut for the logarithm that avoids the finite image of ϕ and our argument is independent of this choice since we will be considering expressions on the form $\exp(\langle f, g \rangle)$. Note that $\phi(c, c) = 1$ implies that terms with $c = d$ are excluded. Note also that if we, for $a \in \mathcal{P}$, denote the indicator function $x \mapsto \begin{cases} 1 & \text{if } x=a \\ 0 & \text{otherwise} \end{cases}$ by $1_a \in \mathcal{P}^*$ then $\exp(\langle 1_a, 1_b \rangle) = \phi(a, b)$.

According to the statement, we assume that the Yang–Baxter equations hold for $\Phi' \neq 0$ and $\mathfrak{X}'_{i,j}$ such that $\mathfrak{X}'_{i,j}\mathfrak{X}'_{j,i} = q^2$ and $\mathfrak{X}'_{i,i} = -q^2$ which, in particular, means that $\mathfrak{X}'_{i,j} \neq 0$. Any other $\mathfrak{X}_{i,j}$ satisfying the same relations can be expressed as $\mathfrak{X}'_{i,j} \cdot \phi(c_i, c_j)$ with ϕ satisfying (3.7). This means that it is enough to show that the states have the same factors of Φ and ϕ . The way these factors appear in the vertex weights of Tables 1, 2, 7 and 8 is described in Table 9.

We start by considering the RRR -equation involving only R_R^R -vertices and label the spins of the edges as in (3.3). We then have the following conservation equations:

$$(3.8) \quad \begin{cases} a + b = i + j \\ j + k = e + f \\ i + c = d + k \end{cases} \quad \begin{cases} b + c = n + l \\ a + n = f + m \\ m + l = d + e \end{cases}$$

Note that both systems of equations imply the same global conservation for boundary edges

$$(3.9) \quad a + b + c = d + e + f.$$

By multiplying the ϕ -contributions from all vertices in the Yang–Baxter equation using Table 9 we get that the total contributions to the left- and right-hand sides are $\exp(\frac{1}{2} \text{LHS}_\phi)$ and $\exp(\frac{1}{2} \text{RHS}_\phi)$, respectively where

$$(3.10) \quad \begin{aligned} \text{LHS}_\phi &= \langle a, b \rangle + \langle i, j \rangle + \langle i, c \rangle + \langle d, k \rangle + \langle j, k \rangle + \langle e, f \rangle \\ \text{RHS}_\phi &= \langle a, n \rangle + \langle m, f \rangle + \langle b, c \rangle + \langle l, n \rangle + \langle m, l \rangle + \langle d, e \rangle. \end{aligned}$$

It is easy to verify by hand as in [BBBG24b] that, modulo the conservation equations (3.8), these are equal (and thus only depend on the boundary edges).

For the Φ -contributions we get the powers

$$(3.11) \quad \begin{aligned} \text{LHS}_\Phi &= \frac{1}{2} (\langle -a - i + b + j \rangle + \langle -i - d + c + k \rangle + \langle -j - e + k + f \rangle) \\ \text{RHS}_\Phi &= \frac{1}{2} (\langle -b - l + c + n \rangle + \langle -a - m + n + f \rangle + \langle -m - d + l + e \rangle) \end{aligned}$$

which, after using the conservation equations (3.8) are both equal to $\langle -a + c - d + f \rangle$.¹

We will now argue that this computation immediately gives us all the other cases of RRR -equations. First note that the expressions for the ϕ and Φ -factors for R_L^L , R_R^L and R_L^R are the same as for R_R^R , except that the spins for the left-moving edges have been negated. This is also true for the conservation equations, which can be expressed as $\pm a \pm b = \pm c \pm d$, where the signs are positive for the spins of right-moving edges and negative for the spins of left-moving edges.

To prove the right-moving RRR -equations we only used the conservation equations, and the properties of the antisymmetric form and the \mathcal{P} -average. This means that since we negate the spins for left-moving edges in both the weights and the conservation equations, the other RRR -equations are just reparametrizations of the R_R^R case, and therefore also hold.

Next we consider the RTT -equation involving only right-moving vertices, where we label the spins of the edges as in (3.2). We then have the same conservation equations (3.8) as before.

Furthermore, we also obtain exactly the same ϕ -factors on each side as we did for the RRR -equation above², and since the conservation equations are the same, the ϕ -factors are equal by the same calculation.

Similarly, the powers of Φ for the left- and right-hand sides are

$$(3.12) \quad \begin{aligned} \text{LHS}_\Phi &= \frac{1}{2} \langle -a - i + b + j \rangle + \langle k \rangle + \langle f \rangle = \langle b - i + k + f \rangle \\ \text{RHS}_\Phi &= \frac{1}{2} \langle -m - d + l + e \rangle + \langle n \rangle + \langle f \rangle = \langle l - d + n + f \rangle \end{aligned}$$

which are both equal to $\langle b + c - d + f \rangle$ by the conservation equations.

As before, we will now argue that these computations also prove the other RTT -equations. Again the expressions for the ϕ and Φ -factors for T_L are the same as for T_R , except that the spins for the left-moving edges have been negated, and the conservation equations for T_L and

¹As mentioned earlier the ϕ and Φ invariance for the Yang–Baxter equations only involving the right-moving model was covered in [BBBG24b] but this case (3.11) had been left out in the proof.

²This is of course easy to compute, but can also be seen by rotating the T -vertices so that they become R -vertices.

T_R are related in the same way. Hence the computations for the remaining RTT -equations are simply reparametrizations of the one above. \square

We note that in the proof, the only assumptions on the weights that are used are the color conservations and the appearance of the ϕ - and Φ -factors as in Table 9.

Lemma 3.8. *Theorem 3.1 holds for a particular the Iwahori specialization of Φ and $\mathfrak{X}_{i,j}$.*

Proof. We use Corollary 3.5 to be able to disregard all Yang–Baxter equations involving R_L^R . Lemma 3.6 then tells us that each case of the remaining Yang–Baxter equations involves at most three colors, and that those must appear on the boundary and therefore be fixed.

For the Iwahori specialization all the remaining vertex weights only depend on the relative order of the colors and not on their absolute index in the palette (like the weights for R_L^R do). This means that it is enough to show that each Yang–Baxter equation is satisfied in the case where the palette size is $m = 3$ independent of the number of rows r .

We have now reduced the problem to checking a fixed, finite number of equalities of elements in the fraction field $\mathbb{C}(z_1, z_2, z_3, v)$ which we have verified with a symbolic computer algebra system (`SageMath`). \square

Together with Proposition 3.7 this finishes the proof of Theorem 3.1.

3.1. Remarks about quantum groups. After proving that our families of lattice models are solvable, let us make a few remarks about quantum groups — an algebraic structure that was developed in connection with seeking solutions to Yang–Baxter equations. For our purposes, we may think of a quantum group \mathcal{A} as a q -deformation of a universal enveloping algebra. There is a special element \mathcal{R} in a completion of the tensor product $\mathcal{A} \otimes \mathcal{A}$ called the *universal R -matrix*. Given three modules U , V and W of \mathcal{A} one can obtain a solution to the Yang–Baxter equation (3.1) from the action of \mathcal{R} on these modules [KS97]. Indeed, the name *universal R -matrix* comes from the fact that solutions to the Yang–Baxter equations are called R -matrices. The matrix coefficients of the action of \mathcal{R} on the corresponding modules are the weights for the R -vertices (and T -vertices) in the lattice models.

The weights for the R_R^R -vertices in this paper come from the R -matrix of a standard evaluation module $V_R(z)$ of a (combinatorial) Drinfeld twist of the affine supersymmetric quantum group $U_q(\widehat{\mathfrak{gl}}(m|1))$ where m is the number of colors [BBBG24b]. The standard evaluation module is defined as $V_R(z) = \mathbb{C}^{m|1} \otimes \mathbb{C}[z, z^{-1}]$ where $\mathbb{C}^{m|1}$ is the standard module of $\mathfrak{gl}(m|1)$.

Drinfeld twists conjugates the universal R -matrix, preserving the Yang–Baxter equation but resulting in slightly different R -matrix solutions. The effects of such a Drinfeld twist on R -vertex weights was derived in [BBBF18, Section 4]. They showed that when two paths of colors c and d cross each other the weight gets multiplied by a factor similar to $\phi(c, d)$ in Proposition 3.7. The Φ -factors in the R_R^R and R_L^L weights similarly appear when a colored path crosses unoccupied edges. By a *combinatorial* Drinfeld twist we mean a transformation of the weights of this type for crossing paths preserving the Yang–Baxter equations. The difference is that we have not confirmed that it amounts to a valid conjugation of the universal R -matrix which is beyond the scope of this paper, and not yet possible for the T -vertices since we there lack a quantum module for the vertical edges as will be further discussed below.

The R -vertices R_Γ^Γ for the Γ metaplectic ice model were shown in [BBB19] to come from Drinfeld twists of $U_q(\widehat{\mathfrak{gl}}(1|m))$ where n was the number of charges, or equivalently the number of supercolors. As explained in [BBBG24b] supercolors are merely a relabelling of colors, and since the R -vertices for the left-moving family of models of this paper are (combinatorial) Drinfeld twists of the Γ metaplectic ice model this should mean that they also come from a Drinfeld twist of $U_q(\widehat{\mathfrak{gl}}(1|n))$ with $n = m$.

It is not clear though what the quantum group interpretation is for mixed models with both left- and right-moving rows, and the mixed R -vertices R_R^L and R_L^R . See [BBG25, Section 8] for a discussion of a potential direction of exploration based on the work therein on the case $m = 1$. See also [BS22, Section 3.4] for a discussion regarding this in the crystal limit.

As mentioned above, it is also not clear in general what the quantum module is for vertical edges, but see the recent paper [BBG25] for the case $m = 1$. The T -vertices include both horizontal and vertical edges, which is why we use a combinatorial proof in Proposition 3.7 for the ϕ -factors. Another reason is that much less is known about the quantum group origins of the Φ -factors, although the weights for R_R^R and R_L^L suggest they come from crossing a color path with an “unoccupied path” as mentioned above, this behaviour is not mirrored for the T -vertices or the mixed R -vertices.

3.2. Solvability of the crystal model. Recall that the fused crystal T -vertices of Tables 5 and 6 were obtained from the Iwahori specialization of the left- and right-moving families of lattice models by taking the crystal limit $v \rightarrow 0$ and restricting to the vertex configurations which have at most one color on the vertical edges (by Lemma 2.2 these are the only configurations that can appear with the type of boundary conditions we are considering). Recall also that the left-moving weights have been multiplied by z to remove the partition function’s dependence on the number of columns.

For the Iwahori specialization we call the left- and right-moving models Δ and Γ , respectively, as seen in Figure 1. These two sets of vertex configurations and weights agree with the Γ and Δ T -vertices of the lattice model in [BS22] which were used to compute Demazure characters and atoms for Sp_{2n} and SO_{2n+1} . Buciumas and Scrimshaw also showed in the above paper that the model is *quasi-solvable* meaning that they found R -vertices of types R_Δ^Δ , R_Γ^Γ , and R_Γ^Δ that satisfy the RTT -equations. However, they were not able to find a suitable R_Δ^Γ matrix. One obstruction they described was that they obtained color loops in their Yang–Baxter equations resulting in a dependence on the number of colors m on one side of the equation while not on the other.

We have shown above that the left- and right-moving non-crystal families of lattice models introduced in this paper are solvable with all four types of R -vertices and we will in this section investigate what happens with these when we take the crystal limit $v \rightarrow 0$.

Recall that the Yang–Baxter equations are still satisfied if we multiply all the weights of a type of R -vertex with a power of v . For each type of R -vertex there is a unique such v -factor such that the weights are finite in the limit $v \rightarrow 0$ and not all zero. We present these limits in Tables 10 and 11. The fused versions (i.e. $k = 1$) of the R_Δ^Δ , R_Γ^Γ and R_Γ^Δ agree with those of [BS22]. For R_Δ^Γ we get a very degenerate case with only one non-zero weight. Indeed, this is not a very interesting solution to the problem of finding R_Δ^Γ posed in [BS22] and it may not fulfill their other requirements. However, it illuminates (at least in the non-crystal version) how the issue of color loops is resolved by telescoping sums as explained in the proof of Proposition 3.4.

Theorem 3.9. *The crystal R -vertices in Tables 10 and 11 and the restricted crystal T -vertices in Tables 5 and 6 satisfy the Yang–Baxter RTT -equations in (3.2) and the RRR -equations in (3.3) for all combinations of row types $X, Y, Z \in \{\Gamma, \Delta\}$.*

Proof. All the weights of $T_\Delta, T_\Gamma, R_\Delta^\Delta, R_\Gamma^\Gamma, R_\Gamma^\Delta$ and R_Δ^Γ for the crystal models can be obtained by taking the weights of $T_L, T_R, R_L^L, R_R^R, R_R^L$ and R_L^R , respectively, specializing to the Iwahori case (2.3), multiplying by 1, 1, $-v$, $-v$, 1 and v^{m+2} , setting $v = 0$, and finally restricting T_Δ and T_Γ to those vertex configurations which have at most one color on the vertical edges.

By Theorem 3.1 all compatible configurations of $T_L, T_R, R_L^L, R_R^R, R_R^L$ and R_L^R satisfy the Yang–Baxter equation, and it is therefore sufficient to show that this is still true after each of the steps above. Firstly, the Yang–Baxter equations hold for every choice of Φ and $\mathfrak{X}_{i,j}$, in particular it holds for the Iwahori specialization. Secondly, multiplying all weights of a particular type (say T_Δ) by the same factor also does not affect the Yang–Baxter equations since both the left- and right-hand side are multiplied by the same constant. Thirdly, since the equations hold for every v , they must in particular hold for $v = 0$.

Next, we need to show that we can restrict T_Δ and T_Γ to the vertex configurations which has at most one color on the vertical edges. This will only affect the RTT -equation (3.2) as that is the only one where the T -vertices appear. So suppose that we have some boundary conditions for (3.2) with at most one color on each edge. Then Lemma 2.2 applied to the lower T -vertex on either side implies that the only internal vertical edge on each side can carry at most one color, and therefore the Yang–Baxter equation holds with this restricted set of vertex configurations.

Finally, recall that the weights in Table 6 are actually given by zT_Δ , i.e. they have been scaled by a factor of z . Again, this does not affect the validity of the Yang–Baxter equations as both sides of each equation are scaled by the same factor. \square

3.3. From Γ - Δ duality to left-right duality. We now prove the duality between the left- and right-moving models as shown in Figure 1.

Theorem 3.10. *For any $\mu = (\mu_1, \dots, \mu_r) \in (\mathbb{Z}_{\geq 0})^r$ with $\mu_1 > \mu_2 > \dots > \mu_r$, any $N \in \mathbb{Z}_{\geq 0}$ such that $Nm \geq \mu_1$, and any $\sigma = (\sigma_1, \dots, \sigma_r) \in \mathcal{P}^r$ we have that*

$$Z_{\mu, \sigma}^R(\mathbf{z}) = \mathbf{z}^N Z_{\mu, w_0 \sigma}^{L, N}(w_0 \mathbf{z}),$$

where w_0 is the longest element of the symmetric group S_r , i.e. the order reversing permutation.

The argument is similar to that used to prove Theorem A.1 in [BBB19].

For the proof we need *mixed* models, which are models where some rows consist of left-moving vertices and the others consist of right-moving vertices. For any $\Theta \in \{L, R\}^r$ we consider a grid with r rows where the i^{th} row consists of vertices of type Θ_i . Similarly to before, the boundary conditions are defined by $\mu \in (\mathbb{Z}_{\geq 0})^r$ and $\sigma = (\sigma_1, \dots, \sigma_r) \in (\mathcal{P}_m)^r$. The top boundary condition is defined by μ in exactly the same way as before, i.e. μ lists the column numbers for which there is a path on the top edge, and the boundary condition for the bottom boundary is still that there are no paths on those edges. For the left and right boundaries, the boundary conditions depend on whether it is a row of left- or right-moving vertices. If $\Theta_i = L$, then the boundary conditions for the i^{th} row are the same as for the left-moving systems, i.e. there is a path on the left-most edge of color σ_i and no path on the right-most edge. Similarly, if $\Theta_i = R$, then there is a path on the right-most edge of color σ_i

Table 10. Configurations and Boltzmann weights for R_{Δ}^{Δ} and R_{Γ}^{Γ} for the fused crystal models, where $i \neq j$ in the multicolored vertex configurations. The R_{Δ}^{Δ} and R_{Γ}^{Γ} weights can be obtained from the R_{Γ}^{Γ} and R_{Δ}^{Δ} weights in Table 7, respectively, by first specializing to the Iwahori case (2.3), then multiplying by $-v$ and finally setting $v = 0$.

R_{Δ}^{Δ} and R_{Γ}^{Γ} (crystal)					
z_2					
z_1					
R_{Δ}^{Δ}	z_2	0	$z_1 - z_2$	z_1	$z_1 - z_2$ if $i > j$
R_{Γ}^{Γ}	z_2	$z_1 - z_2$	0	z_1	$z_1 - z_2$ if $i > j$
z_2					
z_1					
R_{Δ}^{Δ}	z_1	z_2	$\begin{cases} z_2 & \text{if } i < j < k \text{ or } j < k \leq i \text{ or } k \leq i < j \\ z_1 & \text{if } j < i < k \text{ or } i < k \leq j \text{ or } k \leq j < i \end{cases}$		
R_{Γ}^{Γ}	z_2	z_1	$\begin{cases} z_1 & \text{if } i < j < k \text{ or } j < k \leq i \text{ or } k \leq i < j \\ z_2 & \text{if } j < i < k \text{ or } i < k \leq j \text{ or } k \leq j < i \end{cases}$		

Table 11. Configurations and Boltzmann weights for the mixed R_{Γ}^{Δ} and R_{Δ}^{Γ} for the fused crystal models, where $i \neq j$ in the multicolored vertex configurations. The R_{Γ}^{Δ} and R_{Δ}^{Γ} weights can be obtained from the R_{Γ}^{Γ} and R_{Δ}^{Δ} weights in Table 7, respectively, by first specializing to the Iwahori case (2.3), then multiplying by 1 and v^{m+2} , respectively, and finally setting $v = 0$.

R_{Γ}^{Δ} and R_{Δ}^{Γ} (crystal)					
z_2					
z_1					
R_{Γ}^{Δ}	$z_1 - z_2$	z_2	z_2	z_2	z_2 if $j > i$
R_{Δ}^{Γ}	0	0	0	0	z_1 if $j > i$
z_2					
z_1					
R_{Γ}^{Δ}	z_1	z_2	z_2 if $i < j < k$ or $j < k \leq i$ or $k \leq i < j$		
R_{Δ}^{Γ}	0	0	0		

and no path on the left-most edge. We will denote this mixed system by $\mathfrak{S}_{\mu,\sigma}^{\Theta,N}$, where Nm is the number of columns, and abbreviate its partition function as $Z_{\mu,\sigma}^{\Theta,N}(\mathbf{z})$.

The proof of Theorem 3.10 now follows from repeated application of the following two lemmas.

Lemma 3.11. *Let μ , N and σ be as in Theorem 3.10 and $\Theta \in \{\mathbf{L}, \mathbf{R}\}^r$ with $\Theta_i \neq \Theta_{i+1}$ for some i . Then*

$$(3.13) \quad Z_{\mu,\sigma}^{\Theta,N}(\mathbf{z}) = Z_{\mu,s_i\sigma}^{s_i\Theta,N}(s_i\mathbf{z}),$$

where s_i is the i^{th} simple transposition in S_r .

Proof of Lemma 3.11. Without loss of generality we can assume that $\Theta_i = \mathbf{L}$ and $\Theta_{i+1} = \mathbf{R}$. Recall that for the system $\mathfrak{S}_{\mu,\sigma}^{\Theta,N}$ on the left-hand side of (3.13) the boundary conditions for the left boundary edges on rows i and $i+1$ are that their spins are σ_i and unoccupied, respectively. We may therefore consider a new system where we have attached the $R_{\mathbf{R}}^{\mathbf{L}}$ -vertex \times^{σ_i} to the left of these two edges. According to Table 8 there are no other admissible $R_{\mathbf{R}}^{\mathbf{L}}$ -vertex configurations with the same left spins. Thus we may replace the fixed interior spins on the right side of the $R_{\mathbf{R}}^{\mathbf{L}}$ -vertex with free, unspecified spins that are summed over without affecting the partition function, giving us a new system where only the boundary spins are fixed. This can be illustrated as the following equality of partition functions, where the dashed internal edges are summed over and all of the boundary edges are fixed and equal on both systems.

$$(3.14) \quad \begin{array}{c} \text{Diagram 1: A grid with 4 columns and 3 rows. The leftmost edge of row } i \text{ is a blue line with spin } \sigma_i. \text{ The leftmost edge of row } i+1 \text{ is a red line with spin } \sigma_{i+1}. \text{ The rightmost edge of row } i+1 \text{ is a red line with spin } \sigma_{i+1}. \end{array} = \begin{array}{c} \text{Diagram 2: A grid with 4 columns and 3 rows. The leftmost edge of row } i \text{ is a blue line with spin } \sigma_i. \text{ The leftmost edge of row } i+1 \text{ is a red line with spin } \sigma_{i+1}. \text{ The rightmost edge of row } i+1 \text{ is a red line with spin } \sigma_{i+1}. \end{array}$$

Since the weight of the $R_{\mathbf{R}}^{\mathbf{L}}$ -vertex configuration is $\Phi(z_1 - q^2 z_2)$, the partition function of this new system is simply $\Phi(z_1 - q^2 z_2) Z_{\mu,\sigma}^{\Theta,N}(\mathbf{z})$.

We can now apply the Yang–Baxter equation (3.2) to the system on the right-hand side of (3.14) to move the R -vertex one step to the right, which gives us the first equality below. We can then continue this process to move the R -vertex all the way to the right, so that it is attached to the right boundary of the grid. This is sometimes known as the *train argument* and can be illustrated as

$$\begin{array}{c} \text{Diagram 1: A grid with 4 columns and 3 rows. The leftmost edge of row } i \text{ is a blue line with spin } \sigma_i. \text{ The leftmost edge of row } i+1 \text{ is a red line with spin } \sigma_{i+1}. \text{ The rightmost edge of row } i+1 \text{ is a red line with spin } \sigma_{i+1}. \end{array} = \begin{array}{c} \text{Diagram 2: A grid with 4 columns and 3 rows. The leftmost edge of row } i \text{ is a blue line with spin } \sigma_i. \text{ The leftmost edge of row } i+1 \text{ is a red line with spin } \sigma_{i+1}. \text{ The rightmost edge of row } i+1 \text{ is a red line with spin } \sigma_{i+1}. \end{array} = \dots = \begin{array}{c} \text{Diagram 3: A grid with 4 columns and 3 rows. The leftmost edge of row } i \text{ is a blue line with spin } \sigma_i. \text{ The leftmost edge of row } i+1 \text{ is a red line with spin } \sigma_{i+1}. \text{ The rightmost edge of row } i+1 \text{ is a red line with spin } \sigma_{i+1}. \end{array}$$

where again boundary edges are fixed and matching.

Similarly to before, it can be seen in Table 8 that there is only one admissible vertex configuration for the R -vertex in the right-most system, and we can therefore deduce that its partition function is $\Phi(z_1 - q^2 z_2) Z_{\mu,s_i\sigma}^{s_i\Theta,N}(s_i\mathbf{z})$, a multiple of the right-hand side of (3.13). Note that the row types and row parameters of row i and $i+1$ were swapped when the R -vertex moved through the grid.

Hence

$$\Phi(z_1 - q^2 z_2) Z_{\mu, \sigma}^{\Theta, N}(\mathbf{z}) = \Phi(z_1 - q^2 z_2) Z_{\mu, s_i \sigma}^{s_i \Theta, N}(s_i \mathbf{z})$$

as elements of the fraction field \mathcal{F} introduced in Section 2 which implies (3.13). \square

The following lemma shows that the partition function does not depend on the last row type.

Lemma 3.12. *Let μ , N and σ be as in Theorem 3.10 and $\Theta_1, \dots, \Theta_{r-1} \in \{\mathbf{L}, \mathbf{R}\}$. Then*

$$(3.15) \quad Z_{\mu, \sigma}^{(\Theta_1, \dots, \Theta_{r-1}, \mathbf{R}), N}(\mathbf{z}) = z_r^N Z_{\mu, \sigma}^{(\Theta_1, \dots, \Theta_{r-1}, \mathbf{L}), N}(\mathbf{z}).$$

Proof of Lemma 3.12. Consider some state $\mathfrak{s}_{\text{LHS}}$ on the left-hand side of (3.15), i.e. some state where the last row consists of right-moving vertices. Because of the boundary condition, there can only be a single path on the last row, say of color c_i , which comes down from above on some vertical edge, and then goes straight to the right boundary as illustrated in Figure 5. Therefore the only vertex configurations that can appear on the last row are \mathbf{a}_1 , \mathbf{c}_2 and \mathbf{b}_2 .

By changing the type of the last row to be left-moving and changing the path to go to the left instead of to the right, we obtain a state $\mathfrak{s}_{\text{RHS}}$ on the right-hand side of (3.15) as illustrated in Figure 5. The only vertex configurations that can appear on its last row are \mathbf{b}_2 , \mathbf{c}_2 and \mathbf{a}_1 .

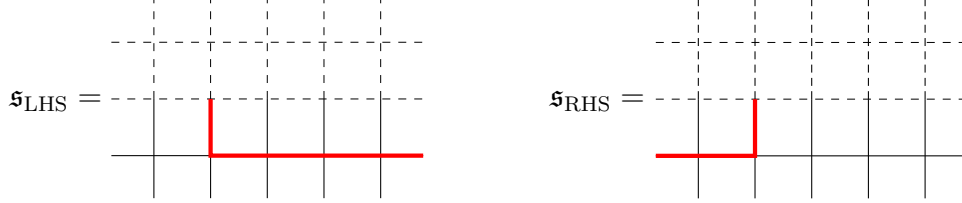


Figure 5. The last row of a right-moving and a left-moving state, respectively.

By multiplying the \mathbf{b}_2 , \mathbf{c}_2 and \mathbf{a}_1 weights of the left-moving model in Table 2 by z whenever the column color c_j is equal to c_i , we obtain precisely the \mathbf{a}_1 , \mathbf{c}_2 and \mathbf{b}_2 weights of the right-moving model in Table 1. Therefore the weight of $\mathfrak{s}_{\text{LHS}}$ is equal to the weight of $\mathfrak{s}_{\text{RHS}}$ multiplied by z_r^N .

This defines a weight-respecting bijection $\mathfrak{S}_{\mu, \sigma}^{(\Theta_1, \dots, \Theta_{r-1}, \mathbf{R}), N} \xrightarrow{\sim} \mathfrak{S}_{\mu, \sigma}^{(\Theta_1, \dots, \Theta_{r-1}, \mathbf{L}), N}$ by $\mathfrak{s}_{\text{LHS}} \mapsto \mathfrak{s}_{\text{RHS}}$ such that $\text{wt}(\mathfrak{s}_{\text{LHS}}) = z_r^N \text{wt}(\mathfrak{s}_{\text{RHS}})$, from which (3.15) follows. \square

Proof of Theorem 3.10. Consider the right-moving system $\mathfrak{S}_{\mu, \sigma}^{\mathbf{R}}(\mathbf{z})$ on the left-hand side of the equality. By Lemma 3.12 we can replace the last row with a left-moving row:

$$Z_{\mu, \sigma}^{\mathbf{R}}(\mathbf{z}) = z_r^N Z_{\mu, \sigma}^{(\mathbf{R}, \dots, \mathbf{R}, \mathbf{L}), N}(\mathbf{z}).$$

We can then repeatedly apply Lemma 3.11 to move the left-moving row to the top:

$$z_r^N Z_{\mu, \sigma}^{(\mathbf{R}, \dots, \mathbf{R}, \mathbf{L}), N}(\mathbf{z}) = z_r^N Z_{\mu, s_{r-1} \sigma}^{(\mathbf{R}, \dots, \mathbf{L}, \mathbf{R}), N}(s_{r-1} \mathbf{z}) = \dots = z_r^N Z_{\mu, w_1 \sigma}^{(\mathbf{L}, \mathbf{R}, \dots, \mathbf{R}), N}(w_1 \mathbf{z}),$$

where $w_1 = s_1 s_2 \dots s_{r-1}$. Then we can use Lemma 3.12 again:

$$z_r^N z_{r-1}^N Z_{\mu, w_1 \sigma}^{(\mathbf{L}, \mathbf{R}, \dots, \mathbf{R}), N}(w_1 \mathbf{z}) = z_r^N z_{r-1}^N Z_{\mu, w_1 \sigma}^{(\mathbf{L}, \mathbf{R}, \dots, \mathbf{R}, \mathbf{L}), N}(w_1 \mathbf{z}),$$

and Lemma 3.11 to move the last row up to the second row:

$$z_r^N z_{r-1}^N Z_{\mu, w_1 \sigma}^{(\mathbf{L}, \mathbf{R}, \dots, \mathbf{R}, \mathbf{L}), N}(w_1 \mathbf{z}) = \dots = z_r^N z_{r-1}^N Z_{\mu, w_2 \sigma}^{(\mathbf{L}, \mathbf{L}, \mathbf{R}, \dots, \mathbf{L}), N}(w_2 \mathbf{z}),$$

where $w_2 = s_2 \dots s_{r-1} s_1 \dots s_{r-1}$.

By repeating this for every row, we will eventually end up with

$$\mathbf{z}^N Z_{\mu, w_0 \sigma}^{\mathbf{L}, N}(w_0 \mathbf{z}),$$

where $w_0 = s_{r-1}(s_{r-2}s_{r-1})(s_{r-3} \dots s_{r-1}) \dots (s_2 \dots s_{r-1})(s_1 \dots s_{r-1})$, the longest element in S_r , which finishes the proof. \square

4. CRYSTAL MODELS AND THE SCHÜTZENBERGER INVOLUTION

In this section we will show that the Γ - Δ duality for the crystal limit refines to a weight-respecting bijection of states based on the Schützenberger involution. Moreover, we show that the individual row exchanges in Lemma 3.11 have a state-by-state interpretation in terms of involutions t_i on Gelfand–Tsetlin patterns defined by Berenstein and Kirillov in [KB95]. Gelfand–Tsetlin patterns are in bijection with semistandard Young tableaux for which the Berenstein–Kirillov involutions are the well-known Bender–Knuth involutions introduced in [BK72]. Applying these involutions in the same order as the row exchanges in Theorem 3.10 gives exactly the Schützenberger involution.

In this section we will only discuss fused models, where a column corresponds to a block in the unfused model. We fix an arbitrary r -tuple of colors which gives the colors on the top boundary of our systems from left to right. Our arguments will not depend on this choice. We will denote mixed systems with the fused crystal configurations and weights from Tables 5 and 6 by $\mathfrak{S}_{\lambda+\rho, \sigma}^\Theta$ where $\Theta \in \{\Gamma, \Delta\}^r$ are the row types, the integer partition $\lambda \in \mathbb{Z}^r$ and $\rho = (r-1, r-2, \dots, 1, 0)$ determine the occupied top boundary fused column numbers, and $\sigma = (\sigma_1, \dots, \sigma_r)$ are the colors for the occupied horizontal boundary edges. Note that $\lambda + \rho$ here gives the fused column numbers instead of the expanded column numbers. We will sometimes consider the union over all possible σ and denote this by $\mathfrak{S}_{\lambda+\rho}^\Theta = \bigsqcup_{\sigma} \mathfrak{S}_{\lambda+\rho, \sigma}^\Theta$. In this section it is important that the systems only contain admissible states (i.e. with non-zero weight). As before we abbreviate the partition functions $Z(\mathfrak{S}_{\lambda+\rho, \sigma}^\Theta)(\mathbf{z})$ and $Z(\mathfrak{S}_{\lambda+\rho}^\Theta)(\mathbf{z})$ to $Z_{\lambda+\rho, \sigma}^\Theta(\mathbf{z})$ and $Z_{\lambda+\rho}^\Theta(\mathbf{z})$, respectively.

4.1. Gelfand–Tsetlin patterns. Recall that with our usual boundary conditions, when we let $v \rightarrow 0$ in the fused Gamma and Delta Iwahori models we can, without affecting the partition function, restrict the model by disallowing all vertical edges with multiple colors. Therefore the top boundary conditions are given by r *distinct* fused column numbers and associated colors from the fixed r -tuple of colors. This is in contrast to the non-crystal limit where there may be multiple paths on the same fused edge on the top boundary, as it corresponds to an entire block.

We will show that the states with top boundary columns given by $\lambda + \rho$ are in bijection with Gelfand–Tsetlin patterns with top row λ . A Gelfand–Tsetlin pattern \mathfrak{T} is a triangular arrangement of non-negative integers

$$(4.1) \quad \mathfrak{T} = \begin{pmatrix} a_{0,0} & & a_{0,1} & & a_{0,2} & \cdots & a_{0,r-1} \\ & a_{1,1} & & a_{1,2} & & \cdots & a_{1,r-1} \\ & & \ddots & & \vdots & \ddots & \\ & & & a_{r-1,r-1} & & & \end{pmatrix}$$

such that each triangle of neighboring integers satisfies the inequalities

$$(4.2) \quad \begin{array}{ccc} a_{i-1,j-1} & & a_{i-1,j} \\ & \searrow & \nearrow \\ & a_{i,j} & \end{array}$$

We denote by GTP_λ the set of Gelfand–Tsetlin patterns with top row $\lambda = (\lambda_1, \dots, \lambda_r)$, that is those satisfying $a_{0,i} = \lambda_{i+1}$ in (4.1). We will also consider the subsets of *left-strict* or *right-strict* Gelfand–Tsetlin patterns where the inequalities in (4.2) are restricted to $a_{i-1,j-1} > a_{i,j} \geq a_{i-1,j}$ or $a_{i-1,j-1} \geq a_{i,j} > a_{i-1,j}$, respectively. As will be shown below, the left-strict Gelfand–Tsetlin patterns are in bijection with the states of the Γ crystal model and the right-strict patterns are in bijection with Δ states. We will therefore also say that these two subsets of Gelfand–Tsetlin patterns are of type Γ and Δ , respectively.

More generally, we say that a pair of consecutive rows in a Gelfand–Tsetlin pattern is of type Γ or Δ if the triangular arrangements of inequalities between these two rows are all left-strict or all right-strict, respectively. We may consider subsets of Gelfand–Tsetlin patterns with mixed row-pair types specified by a list $\Theta' = (\Theta'_1, \dots, \Theta'_{r-1})$ where $\Theta'_i \in \{\Gamma, \Delta\}$ counting from top to bottom. We denote these subsets by $\text{GTP}_\lambda^{\Theta'} \subset \text{GTP}_\lambda$. Note that they are not disjoint. Note also that the list of row-pair types Θ' has length $r - 1$ while the list of row types Θ for lattice models defined in Section 3.3 has length r . These are related in the following proposition which proves that the set of admissible mixed states with row types $\Theta = (\Theta_1, \dots, \Theta_r)$ and top row boundary condition $\lambda + \rho$ is in bijection with the set of Gelfand–Tsetlin patterns with r rows, row-pair types $\Theta' = (\Theta_1, \dots, \Theta_{r-1})$ and top row $\lambda + \rho$. Later, in Proposition 4.3 we show that this bijection preserves the notion of weight (which we define for Gelfand–Tsetlin patterns below).

Proposition 4.1. *Fix a list of row types $\Theta = (\Theta_1, \dots, \Theta_r) \in \{\Gamma, \Delta\}^r$ and let $\Theta' = (\Theta_1, \dots, \Theta_{r-1})$. There is a bijection $\iota_\Theta : \mathfrak{S}_{\lambda+\rho}^\Theta \rightarrow \text{GTP}_{\lambda+\rho}^{\Theta'}$.*

For similar statements for other lattice models see for example [BBF11a, BBC⁺12]. From now on, we write the truncation of a list row types $\Theta = (\Theta_1, \dots, \Theta_{r-1}, \Theta_r)$ to a list of row-pair types as $\Theta' = (\Theta_1, \dots, \Theta_{r-1})$.

Remark 4.2. As we will see in the proof, the Gelfand–Tsetlin pattern does not carry any information about the colors of the paths in the lattice model state; it only depends on the positions of the fused vertical edges the paths occupy. Recall that the fused columns do not restrict which colors their edges can carry, unlike the unfused columns. However, the color information is not lost since given the layouts of the paths and given the fixed top boundary colors we show that there is a unique way of coloring the paths for the crystal model. The notion of an uncolored state can be obtained by considering a palette with only a single color, say gray, which we think of as *occupied*. This deterministic feature is not shared with the Iwahori model for general $v \neq 0$ as can be seen for example in Figure 2a where we can swap red and green between the second and third row.

Proof of Proposition 4.1. Suppose we have some mixed state \mathfrak{s} with row types Θ and top boundary condition given by $\lambda + \rho$. Recall that \mathfrak{s} has r rows indexed from 1 to r starting from the top, that there are r paths starting from the top boundary, and that on each row one path exits the lattice to either the right or left depending on Θ . Therefore there will be paths on r of the vertical edges at the top, on $r - 1$ of the vertical edges directly below

the first row, and so on. We can then define a Gelfand–Tsetlin pattern \mathfrak{T} by setting the row with index $0 \leq i \leq r-1$ to be the column numbers of the occupied vertical edges below row i in the lattice, taken from left to right. In particular, for $i=0$ this means that we set $a_{0,j} = (\lambda + \rho)_j$ by imagining a zeroth row above the top boundary. Recall that the column numbers are decreasing from left to right so that, by definition, each row in \mathfrak{T} is strictly decreasing.

For any $1 \leq i \leq r-1$, to see that the necessary inequalities for the row-pair $(i-1, i)$ in \mathfrak{T} are satisfied, suppose first that $\Theta_i = \Gamma$, i.e. that the i^{th} row of \mathfrak{s} is a Gamma row. Recall that for a Gamma vertex we consider the top and left edges to be inputs, and the bottom and right edges to be outputs.

We have to check the two inequalities coming from the left-strict version of (4.2): (i) $a_{i-1,j-1} > a_{i,j}$ and (ii) $a_{i,j} \geq a_{i-1,j}$ for every j . For (i), suppose instead that $a_{i-1,j-1} \leq a_{i,j}$ for some j . Consider the section of vertices on the i^{th} row that are left of column $a_{i,j}$, including the vertex on column $a_{i,j}$ itself, together with their edges. The number of occupied bottom (top) edges in this section is given by the number of entries in \mathfrak{T} on row i (row $i-1$) that are larger than or equal to $a_{i,j}$. If $a_{i-1,j-1} < a_{i,j}$, this means that there are strictly fewer occupied edges at the top than at the bottom of the section, since the rows in \mathfrak{T} are strictly decreasing. The boundary conditions imply that the left boundary edge of the section is unoccupied, and thus the number of ingoing paths is strictly smaller than the number of outgoing paths for the section, regardless of the occupancy of its right boundary edge, contradicting the fact that the number of paths has to be preserved for this section.

If, on the other hand, $a_{i-1,j-1} = a_{i,j}$, then there are as many paths coming in from the top as there are going out via the bottom boundary. However, the right-most vertex of the section (at column $a_{i,j}$) must have both top and bottom edges occupied, and so has to be of type \mathbf{a}_2 or \mathbf{a}'_2 . This means that there must be an additional path going out to the right, but, as before, none coming in from the left, which again leads to a contradiction of path preservation.

For (ii), suppose for a contradiction that $a_{i,j} < a_{i-1,j}$. We proceed similarly to above, but instead consider the section of vertices on the i^{th} row that are *right* of column $a_{i,j}$, including the vertex on column $a_{i,j}$ itself. The number of occupied bottom (top) edges in this section is given by the number of entries in \mathfrak{T} on row i (row $i-1$) that are *smaller* than or equal to $a_{i,j}$. If $a_{i,j} < a_{i-1,j}$, this means that there are strictly fewer occupied edges at the top than at the bottom of the section. The boundary conditions imply that the right boundary edge of the section is occupied, and thus the number of ingoing paths is strictly smaller than the number of outgoing paths for the section, regardless of the occupancy of its left boundary edge, giving a contradiction.

The Δ case is similar, and hence \mathfrak{T} is a Gelfand–Tsetlin pattern with row-pair types Θ' .

Conversely, given a Gelfand–Tsetlin pattern \mathfrak{T} with r rows, row-pair types Θ' and top row $\lambda + \rho$ we can define an admissible state \mathfrak{s} as follows. We will first specify which edges are occupied without considering colors and then show that there is only one way to assign colors to the occupied edges to obtain an admissible state with the fixed top boundary colors.

For every $0 \leq i \leq r-1$ and $i \leq j \leq r-1$, let the vertical edge in column $a_{i,j}$ below row i in the lattice be occupied. Then fill in the horizontal edges in each row i of \mathfrak{s} by adding a horizontal uncolored path from each top vertical edge to the next bottom vertical edge, or the boundary, to the right if $\Theta_i = \Gamma$, or to the left if $\Theta_i = \Delta$. Because of the left-strict and

right-strict Gelfand–Tsetlin inequalities, the paths will neither overlap (i.e. occupy the same edge) nor go straight down, so we get an uncolored state whose only vertex configurations are the uncolored versions of those in Table 5 for Γ rows and those in Table 6 for Δ rows.

Now note that given an uncolored version of one of these vertex configurations and a coloring of its occupied input edges, there is a unique way to color the occupied output edges such that the resulting vertex configuration becomes admissible. The colors of the top boundary edges are given. For each row, the left or right boundary edge is unoccupied for row type Γ or Δ , respectively. This means that we know the colors of the occupied input edges of the top left or top right vertex, respectively, and can therefore deduce the colors of its occupied output edges. By proceeding iteratively along the row we can assign unique colors to each occupied horizontal edge as well as each occupied vertical edge directly below the row. We can then continue downwards row by row until every occupied edge has been colored. \square

The weight $\text{wt}(\mathfrak{T})$ of a Gelfand–Tsetlin pattern \mathfrak{T} with r rows is defined as the list $(d_{r-1}, d_{r-2} - d_{r-1}, \dots, d_0 - d_1)$ of differences of consecutive row sums from the bottom up

$$(4.3) \quad d_i = \sum_{j=i}^{r-1} a_{i,j}.$$

The first entry can also be interpreted as a difference of consecutive row sums if we imagine that there is an extra empty row below the $(r-1)^{\text{th}}$ row, so that $d_r = 0$.

Proposition 4.3. *Let $\Theta \in \{\Gamma, \Delta\}^r$ and $\mathfrak{T} \in \text{GTP}_{\lambda+\rho}^{\Theta'}$. If $\mathfrak{s} = \iota_{\Theta}^{-1}(\mathfrak{T})$ is the state in $\mathfrak{S}_{\lambda+\rho}^{\Theta}$ associated to \mathfrak{T} by Proposition 4.1, then*

$$(4.4) \quad \text{wt}(\mathfrak{s})(\mathbf{z}) = \mathbf{z}^{w_0 \text{ wt}(\mathfrak{T})},$$

where w_0 is the longest element of the symmetric group S_r , i.e. the order reversing permutation.

In particular, this means that the weight $\text{wt}(\mathfrak{s})(\mathbf{z}) = \text{wt}(\iota_{\Theta}^{-1}(\mathfrak{T}))(\mathbf{z})$ does not depend on the last row type Θ_r (which should be familiar from the general left-right duality in Section 3.3).

Proof. First note from Tables 5 and 6 that the left-hand side is a monomial in z_1, \dots, z_r . Furthermore, the exponent of z_i is determined by the weight of the i^{th} row in \mathfrak{s} , and it is therefore sufficient to show that this weight is equal to

$$z_i^{d_{i-1} - d_i},$$

where d_i is the sum of the i^{th} row of the Gelfand–Tsetlin pattern as above (where again we interpret d_r as 0). We only present the proof for $i < r$; the remaining case $i = r$ is essentially the same but with some obvious modifications due to the fact that there is no row indexed by r in the Gelfand–Tsetlin pattern.

First consider the case when $\Theta_i = \Gamma$. We can see in Table 5 that the admissible Γ weights are either 1 or z_i for row i , and that a vertex configuration has weight z_i precisely when its left edge is occupied. So the exponent of z_i is equal to the number of vertices on row i with occupied left-edges, which in turn is equal to the number of occupied internal horizontal edges (since there is no path on the left boundary). On row i there are a number of paths coming in from above at the columns numbered $a_{i-1,i-1}, \dots, a_{i-1,r-1}$, by the definition of \mathfrak{s} in the proof of Proposition 4.1. Furthermore, all but one path leave the row via the bottom edges at the columns numbered $a_{i,i}, \dots, a_{i,r-1}$, and the remaining path goes out to the right

boundary. Hence the number of occupied internal horizontal edges on row i is the summed differences of these column numbers, namely

$$\sum_{j=i-1}^{r-1} a_{i-1,j} - \sum_{j=i}^{r-1} a_{i,j},$$

which is what we wanted to show.

For the case when $\Theta_i = \Delta$ we can similarly see from Table 6 that the exponent of z_i is equal to the number of vertices on row i with *unoccupied* left-edges, which in turn is equal to the number of unoccupied internal horizontal left-edges (since the left boundary edge is occupied). Again, on row i in the lattice there are a number of paths coming in from above at the columns numbered $a_{i-1,i-1}, \dots, a_{i-1,r-1}$ and all but one path leave the row via the bottom edges at the columns numbered $a_{i,i}, \dots, a_{i,r-1}$, while the remaining path goes out to the left boundary at column number N . Hence the number of occupied internal horizontal edges on row i is $(N + \sum_{j=i}^{r-1} a_{i,j}) - \sum_{j=i-1}^{r-1} a_{i-1,j}$, which means that the number of *unoccupied* such edges is

$$\sum_{j=i-1}^{r-1} a_{i-1,j} - \sum_{j=i}^{r-1} a_{i,j},$$

which is what we wanted to show. \square

4.2. Berenstein–Kirillov involutions. We now define the Berenstein–Kirillov involutions on Gelfand–Tsetlin patterns introduced in [KB95] and mentioned earlier in this section, but using the index conventions of [BBF11b]. Let the entries $a_{i,j}$ of a rank r Gelfand–Tsetlin pattern be indexed as in (4.1) such that $i \in \{0, \dots, r-1\}$ enumerates the rows from top to bottom. There are $r-1$ Berenstein–Kirillov involutions, and each involution acts on a single row $i \in \{1, \dots, r-1\}$ of the pattern, leaving the remaining rows unchanged. This means that there is one involution acting on each row except for the top row and due to differing indexing conventions the involution that acts on row i is denoted t_{r-i} for $i \in \{1, \dots, r-1\}$.

To describe the action of the Berenstein–Kirillov involution t_{r-i} , first note that the defining inequalities of the Gelfand–Tsetlin patterns restrict every entry $a_{i,j}$ to the interval with upper bound given by the minimum of the left diagonal entries and lower bound given by the maximum of the right diagonal entries. The involution t_{r-i} is then given by reflecting each entry $a_{i,j}$ on the i^{th} row in its admissible interval, that is, replacing $a_{i,j}$ by

$$(4.5) \quad a'_{i,j} = \min(a_{i-1,j-1}, a_{i+1,j}) + \max(a_{i-1,j}, a_{i+1,j+1}) - a_{i,j}.$$

When $j = i$ or $j = r-1$, that is when $a_{i,j}$ is on one of the diagonals, we interpret the first and second terms as $a_{i-1,j-1}$ and $a_{i-1,j}$, respectively. An example is given in Figure 6.

In terms of lattice models, we will show that by interpreting the Gelfand–Tsetlin patterns as mixed states by Proposition 4.1, these Berenstein–Kirillov involutions can be thought of as swapping a Gamma and a Delta row, just like the mixed R -matrix did in Section 3.3. In this way we obtain a state-by-state refinement not only of the complete Gamma–Delta duality, but of each individual step.

There is a well-known bijection between Gelfand–Tsetlin patterns $\mathfrak{T} \in \text{GTP}_\lambda$ and semistandard Young tableaux $T \in \text{SSYT}(\lambda)$ such that the rows of \mathfrak{T} define consecutive shapes of T with increasing box contents. Under this bijection the Berenstein–Kirillov involutions t_i are the Bender–Knuth involutions BK_i on semistandard Young tableaux introduced in [BK72].

Another involution q_i of Gelfand–Tsetlin patterns can be defined recursively by $q_i = q_{i-1}t_i \cdots t_2t_1$ for $i \in \{1, \dots, r-1\}$ with $q_0 = 1$, and then q_{r-1} coincides with the Schützenberger involution on semistandard Young tableaux by [KB95, Theorem 2.1]. The other q_i involutions are called partial Schützenberger involutions.

Since the Berenstein–Kirillov involution t_{r-i} only acts and depends on rows $i-1$, i and $i+1$ of a Gelfand–Tsetlin pattern (if these rows exist) it is often convenient to restrict our attention to three such rows. We call three consecutive rows of some Gelfand–Tsetlin pattern a *short pattern* \mathbf{t} and we will use the following parametrization of its entries

$$(4.6) \quad \mathbf{t} = \left\{ \begin{array}{cccccc} x_0 & x_1 & x_2 & \cdots & x_{\ell+1} & x_{\ell+2} \\ & y_0 & y_1 & \cdots & & y_{\ell+1} \\ & & z_0 & z_1 & \cdots & z_\ell \end{array} \right\}.$$

Mirroring the definition for Gelfand–Tsetlin patterns, we define the weight of a short pattern to be the pair consisting of the two differences of consecutive row sums, i.e.

$$\text{wt}(\mathbf{t}) = \left(\sum_{i=0}^{l+1} y_i - \sum_{i=0}^l z_i, \sum_{i=0}^{l+2} x_i - \sum_{i=0}^{l+1} y_i \right).$$

We also define an involution t_{short} on short patterns, acting like a Berenstein–Kirillov involution on the middle row.

Recall from Proposition 4.1 that mixed lattice model states are in bijection with Gelfand–Tsetlin patterns with corresponding row-pair types. We will now show how the Berenstein–Kirillov involutions on Gelfand–Tsetlin patterns can be naturally transferred to involutions on lattice model states. More precisely, for any $\Theta = (\Theta_1, \dots, \Theta_r)$ with $\Theta_i \neq \Theta_{i+1}$ we will show that we have a commuting diagram of bijections:

$$(4.7) \quad \begin{array}{ccccccc} \mathfrak{S}_{\lambda+\rho}^{\Theta} & \xleftarrow{\iota_{\Theta}} & \text{GTP}_{\lambda+\rho}^{\Theta'} & \xleftarrow{\vartheta_{\Theta'}} & \text{GTP}_{\lambda} & \longleftrightarrow & \text{SSYT}(\lambda) \\ \updownarrow & & \updownarrow t_{r-i} & & \updownarrow t_{r-i} & & \updownarrow \text{BK}_{r-i} \\ \mathfrak{S}_{\lambda+\rho}^{s_i\Theta} & \xleftarrow{\iota_{s_i\Theta}} & \text{GTP}_{\lambda+\rho}^{(s_i\Theta)'} & \xleftarrow{\vartheta_{(s_i\Theta)'}} & \text{GTP}_{\lambda} & \longleftrightarrow & \text{SSYT}(\lambda) \end{array}$$

Here the left-most horizontal bijection ι_{Θ} was defined in Proposition 4.1, the middle horizontal bijection $\vartheta_{\Theta'}$ will be defined below and proved to be a bijection in Lemma 4.5, and the right-most bijection is well-known. Every t_{r-i} preserves the top row of a Gelfand–Tsetlin pattern, and therefore t_{r-i} maps GTP_{λ} to itself, giving the third vertical bijection. In Lemma 4.6 we will show that t_{r-i} also maps the subset $\text{GTP}_{\lambda+\rho}^{\Theta'}$ to $\text{GTP}_{\lambda+\rho}^{(s_i\Theta)'}$, which gives the second vertical bijection, and also show that the middle square commutes. Finally, we define the new dashed vertical map between lattice model states (which we will also call t_{r-i}) from the involution on Gelfand–Tsetlin patterns such that the left-most square commutes.

For a fixed list of row-pair types $\Theta' \in \{\Gamma, \Delta\}^{r-1}$ we define the map $\vartheta_{\Theta'} : \text{GTP}_{\lambda} \rightarrow \text{GTP}_{\lambda+\rho}^{\Theta'}$ as follows. For any $\mathfrak{T} \in \text{GTP}_{\lambda}$ with entries $a_{i,j}$ as in (4.1), we define the entries $b_{i,j}$ of $\vartheta_{\Theta'}(\mathfrak{T})$ to be

$$(4.8) \quad b_{i,j} = a_{i,j} + \rho_{i,j}^{\Theta'},$$

where $\rho^{\Theta'}$ is the unique element of $\text{GTP}_{\lambda+\rho}^{\Theta'}$ with smallest possible non-negative entries. This $\rho^{\Theta'}$ can be constructed by taking a copy of the row vector $\rho = (r-1, r-2, \dots, 0)$ for the

first row, and for each successive row i (starting from 1) copy the entries on the previous row and truncate it by removing the left-most entry if $\Theta'_i = \Gamma$ and the right-most entry if $\Theta'_i = \Delta$.

Example 4.4. Let $r = 4$ and $\Theta' = (\Gamma, \Delta, \Delta)$. Then $\rho^{\Theta'}$ is the Gelfand–Tsetlin pattern

$$\left\{ \begin{array}{ccccc} 3 & 2 & 1 & 0 & \\ & 2 & 1 & 0 & \\ & & 2 & 1 & \\ & & & 2 & \end{array} \right\}.$$

Lemma 4.5. *The map $\vartheta_{\Theta'} : \text{GTP}_{\lambda} \rightarrow \text{GTP}_{\lambda+\rho}^{\Theta'}$ is a bijection.*

Proof. The map $\vartheta_{\Theta'}$ is clearly injective, so it is sufficient to prove that it is also surjective, i.e. that if $\mathfrak{T} \in \text{GTP}_{\lambda+\rho}^{\Theta'}$ then $\mathfrak{T} - \rho^{\Theta'} \in \text{GTP}_{\lambda}$. We thus need to show that, for any $1 \leq i \leq r-1$, the necessary Gelfand–Tsetlin inequalities for the row-pair $(i-1, i)$ in $\mathfrak{T} - \rho^{\Theta'}$ are satisfied. We will present the case when $\Theta'_i = \Gamma$ in detail; the other case $\Theta'_i = \Delta$ is analogous. If we denote the entries of \mathfrak{T} by $a_{i,j}$ as in (4.1), then by definition we have that

$$a_{i-1,j-1} > a_{i,j} \geq a_{i-1,j}.$$

Because the entries of \mathfrak{T} are integers and $\rho_{i-1,j-1}^{\Theta'} = \rho_{i,j}^{\Theta'} + 1$, it follows from the first inequality that $a_{i-1,j-1} - \rho_{i-1,j-1}^{\Theta'} \geq a_{i,j} - \rho_{i,j}^{\Theta'}$. Furthermore, the second inequality together with the fact that $\rho_{i,j}^{\Theta'} = \rho_{i-1,j}^{\Theta'}$ implies that $a_{i,j} - \rho_{i,j}^{\Theta'} \geq a_{i-1,j} - \rho_{i-1,j}^{\Theta'}$. Thus, the necessary Gelfand–Tsetlin inequalities for the row-pair $(i-1, i)$ in $\mathfrak{T} - \rho^{\Theta'}$ are satisfied.

Together with the analogous arguments for the case $\Theta'_i = \Delta$ this shows that $\mathfrak{T} - \rho^{\Theta'} \in \text{GTP}_{\lambda}$. \square

The following lemma shows how t_{r-i} descends from a map on $\text{GTP}_{\lambda+\rho}$ to a map between subsets $\text{GTP}_{\lambda+\rho}^{\Theta'}$ and why the bijection $\vartheta_{\Theta'}$ is natural.

Lemma 4.6. *Let $\Theta \in \{\Gamma, \Delta\}^r$ and $\mathfrak{T} \in \text{GTP}_{\lambda+\rho}^{\Theta'}$ where $\Theta' \in \{\Gamma, \Delta\}^{r-1}$ is the truncation of Θ . Fix a row $1 \leq i \leq r-1$ such that $\Theta_i \neq \Theta_{i+1}$. Then $t_{r-i}\mathfrak{T} \in \text{GTP}_{\lambda+\rho}^{(s_i\Theta)'}$ and we have the following commuting diagram*

$$(4.9) \quad \begin{array}{ccc} \text{GTP}_{\lambda+\rho}^{\Theta'} & \xleftarrow[\vartheta_{\Theta'}]{\sim} & \text{GTP}_{\lambda} \\ \updownarrow t_{r-i} & & \updownarrow t_{r-i} \\ \text{GTP}_{\lambda+\rho}^{(s_i\Theta)'} & \xleftarrow[\vartheta_{(s_i\Theta)'}]{\sim} & \text{GTP}_{\lambda} \end{array}$$

Proof. We will show the argument for $i < r-1$. The case $i = r-1$ is the same but with some obvious modifications due to the fact that it is the last row.

If $\mathfrak{T} \in \text{GTP}_{\lambda+\rho}^{\Theta'}$, then we already know that $t_{r-i}\mathfrak{T} \in \text{GTP}_{\lambda+\rho}$, but it remains to be shown that it has row-pair types $(s_i\Theta)'$. The involution t_{r-i} only affects the entries of \mathfrak{T} at the i^{th} row, which means that it can only affect the i^{th} and $(i+1)^{\text{th}}$ row-pair types. We can therefore focus on the rows indexed $i-1, i$ and $i+1$. Since $\Theta_i \neq \Theta_{i+1}$ there are two cases: First, if $\Theta_i = \Gamma$ and $\Theta_{i+1} = \Delta$, the row-pair $(i-1, i)$ is left-strict and the row-pair $(i, i+1)$

is right-strict, and thus these three rows look as follows:

$$(4.10) \quad \left\{ \begin{array}{ccccccc} a_{i-1,i-1} & & & a_{i-1,i} & & & a_{i-1,i+1} \\ & > & & \geq & & & \\ & & a_{i,i} & & & a_{i,i+1} & \dots \\ & & & \geq & & & \\ & & & & a_{i+1,i+1} & & a_{i+1,i+2} \end{array} \right\}$$

Second, if $\Theta_i = \Delta$ and $\Theta_{i+1} = \Gamma$, the first row-pair is right-strict and the second row-pair is left-strict, giving:

$$(4.11) \quad \left\{ \begin{array}{ccccccc} a_{i-1,i-1} & & & a_{i-1,i} & & & a_{i-1,i+1} \\ & \geq & & & \geq & & \\ & & a_{i,i} & & & a_{i,i+1} & \dots \\ & & & & & & \\ & & & & a_{i+1,i+1} & & a_{i+1,i+2} \end{array} \right\}$$

Recall that t_{r-i} acts on an entry $a_{i,j}$ by reflecting it in its admissible interval, which (away from the boundary diagonals) is given by $[\min(a_{i-1,j-1}, a_{i+1,j}), \max(a_{i-1,j}, a_{i+1,j+1})]$ and on the boundary by a similar expression (see after (4.5)). Thus, the strict inequalities in (4.10) and (4.11) are also reflected and hence t_{r-i} is a bijection between $\text{GTP}_{\lambda+\rho}^{\Theta'}$ and $\text{GTP}_{\lambda+\rho}^{(s_i\Theta)'}.$

We will now prove that the diagram commutes for the case when $\Theta_i = \Gamma$ and $\Theta_{i+1} = \Delta$; the other case is similar. Start in the upper right corner of (4.9) with some $\mathfrak{T} \in \text{GTP}_{\lambda}$. For an entry $a_{i,j}$ not on the boundary (i.e. $i < j < r-1$), consider the subpattern of \mathfrak{T} consisting of the entry $a_{i,j}$ together with its diagonally adjacent entries, i.e.

$$(4.12) \quad \begin{array}{ccc} a_{i-1,j-1} & & a_{i-1,j} \\ & a_{i,j} & \\ a_{i+1,j} & & a_{i+1,j+1} \end{array}$$

Since $\Theta_i = \Gamma$ and $\Theta_{i+1} = \Delta$, applying the map $\vartheta_{\Theta'}$ to \mathfrak{T} transforms this subpattern to

$$\begin{array}{ccc} a_{i-1,j-1} + (k+1) & & a_{i-1,j} + k \\ & a_{i,j} + k & \\ a_{i+1,j} + (k+1) & & a_{i+1,j+1} + k \end{array}$$

for some integer k that depends on i, j and $\Theta_1, \dots, \Theta_{i-1}$. By the definition in (4.5), applying t_{r-i} to \mathfrak{T} turns the middle entry into

$$\begin{aligned} (a_{i,j} + k)' &= \min(a_{i-1,j-1} + (k+1), a_{i+1,j} + (k+1)) \\ &\quad + \max(a_{i-1,j} + k, a_{i+1,j+1} + k) - (a_{i,j} + k) \\ &= (k+1) + \min(a_{i-1,j-1}, a_{i+1,j}) + \max(a_{i-1,j}, a_{i+1,j+1}) - a_{i,j} \\ &= (k+1) + a'_{i,j}. \end{aligned}$$

If we instead go down and then left in the diagram, the middle entry of the subpattern in (4.12) turns first into $a'_{i,j}$ and then into $a'_{i,j} + (k+1)$, where the integer k is the same as the one above because s_i leaves $\Theta_1, \dots, \Theta_{i-1}$ unchanged.

If the entry $a_{i,j}$ is on a boundary, then $a_{i+1,j}$ or $a_{i+1,j+1}$ does not exist. In the definition of t_{r-i} this is mirrored by removing the corresponding entry or entries appearing inside the min or max in the expression for the interval, and the proof follows analogously. \square

As a result of Proposition 4.1 and Lemma 4.6, we can transfer the Berenstein–Kirillov involution t_{r-i} to a bijection $t_{r-i} : \mathfrak{S}_{\lambda+\rho}^{\Theta} \xrightarrow{\sim} \mathfrak{S}_{\lambda+\rho}^{s_i\Theta}$ of lattice model states, where λ is any partition and Θ is any list of row-types satisfying $\Theta_i \neq \Theta_{i+1}$. This completes the commuting diagram in (4.7) and we give an example in Figure 6.

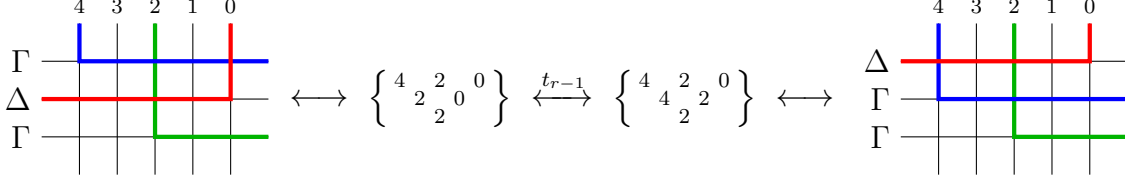


Figure 6. An example of a mixed state in $\mathfrak{S}_{\lambda+\rho}^{\Theta}$ with row types $\Theta = (\Gamma, \Delta, \Gamma)$ and its associated Gelfand–Tsetlin pattern in $\text{GTP}_{\lambda+\rho}^{\Theta'}$ and how these transform under the Berenstein–Kirillov involution t_{r-1} where $r = 3$ acting on the middle row to obtain a state with row types $s_1\Theta = (\Delta, \Gamma, \Gamma)$.

We would also like to know how this new bijection t_{r-i} on lattice model states changes the Boltzmann weights of the states, which is the content of the following theorem.

Theorem 4.7. *For a state $\mathfrak{s} \in \mathfrak{S}_{\lambda+\rho}^{\Theta}$ (where $\Theta_i \neq \Theta_{i+1}$) we have that $\text{wt}(t_{r-i}\mathfrak{s})(\mathbf{z}) = \text{wt}(\mathfrak{s})(s_i\mathbf{z})$.*

The theorem follows from Proposition 4.3 and Corollary 4.9 below.

Lemma 4.8. *If \mathfrak{t} is a short pattern and $\text{wt}(\mathfrak{t}) = (w_2, w_1)$, then $\text{wt}(t_{\text{short}}\mathfrak{t}) = (w_1, w_2)$.*

Proof. Let d_0 , d_1 and d_2 be the sums of the entries on the first, second and third row of \mathfrak{t} . The short pattern $t_{\text{short}}\mathfrak{t}$ will have the same row sum for the first and third row, but its second row sum might be different, so call it d'_1 .

If we label the entries as in (4.6), then by the definition of t_{short} we have that

$$\begin{aligned}
d'_1 &= \sum_{j=0}^{l+1} y'_j = (x_0 + \max(x_1, z_0) - y_0) + \sum_{j=1}^l (\min(x_j, z_{j-1}) + \max(x_{j+1}, z_j) - y_j) \\
&\quad + (\min(x_{l+1}, z_l) + x_{l+2} - y_{l+1}) \\
&= x_0 + x_{l+2} + \sum_{j=0}^l (\min(x_{j+1}, z_j) + \max(x_{j+1}, z_j)) - \sum_{j=0}^{l+1} y_j \\
&= x_0 + x_{l+2} + \sum_{j=0}^l (x_{j+1} + z_j) - \sum_{j=0}^{l+1} y_j \\
&= \sum_{j=0}^{l+2} x_j + \sum_{j=0}^l z_j - \sum_{j=0}^{l+1} y_j = d_0 - d_1 + d_2.
\end{aligned}$$

Then

$$\text{wt}(t_{\text{short}}\mathfrak{t}) = (d'_1 - d_2, d_0 - d'_1) = (d_0 - d_1, d_1 - d_2) = (w_1, w_2). \quad \square$$

Corollary 4.9. *If \mathfrak{T} is a Gelfand–Tsetlin pattern with r rows, then*

$$\text{wt}(t_{r-i}\mathfrak{T}) = s_{r-i} \text{wt}(\mathfrak{T})$$

for any $1 \leq i < r$, where $s_{r-i} \in S_r$ is a simple transposition.

Proof. If $i < r-1$, then this follows from Lemma 4.8 by looking at the short pattern consisting of row $i-1$, i and $i+1$. Because of the order of the entries in $\text{wt}(\mathfrak{T})$, where the first entry of the weight is the bottom row sum, we get s_{r-i} instead of s_i .

If $i = r-1$, for which $t_{r-i} = t_1$ acts on the bottom row with a single entry, then this can be proved analogously to Lemma 4.8. Indeed, consider the last two rows of \mathfrak{T} :

$$\begin{array}{ccc} \ddots & \vdots & \ddots \\ & x_0 & x_1 \\ & & y_0 \end{array}$$

The map t_1 will only change this by replacing the last entry with

$$y'_0 := x_0 + x_1 - y_0$$

and so the first two entries of $\text{wt}(t_1\mathfrak{T})$ are

$$\begin{aligned} y'_0 &= x_0 + x_1 - y_0 \\ (x_0 + x_1) - y'_0 &= y_0, \end{aligned}$$

which is the second and first entry of $\text{wt}(\mathfrak{T})$, respectively. □

Together with Proposition 4.3 this finishes the proof of Theorem 4.7.

So far in this section we have not considered the colors on the left and right boundary edges, only which edges are occupied. To show that the Berenstein–Kirillov involutions are state-by-state refinements of the steps taken in the proof of the Γ - Δ (or left-right) duality that we showed using Yang–Baxter equations in Section 3.3 we also need to show that the colors in the boundary conditions are interchanged.

Theorem 4.10. *The map $t_{r-i} : \mathfrak{S}_{\lambda+\rho}^{\Theta} \rightarrow \mathfrak{S}_{\lambda+\rho}^{s_i\Theta}$ (where $\Theta_i \neq \Theta_{i+1}$) descends to a map $t_{r-i} : \mathfrak{S}_{\lambda+\rho,\sigma}^{\Theta} \rightarrow \mathfrak{S}_{\lambda+\rho,s_i\sigma}^{s_i\Theta}$.*

For this we need to show that if $\mathfrak{s} \in \mathfrak{S}_{\lambda+\rho,\sigma}^{\Theta}$ then the boundary colors of $t_{r-i}(\mathfrak{s}) = \iota_{s_i\Theta}^{-1} \circ t_{r-i} \circ \iota_{\Theta}(\mathfrak{s})$ are given by $s_i\sigma$, which is the purpose of the next section.

Before we begin the proof, let us first compare with the proof of the duality at the level of partition functions in Theorem 3.10, which built on two equalities of partition functions from Lemmas 3.11 and 3.12. The above bijection is a refinement of the equality in Lemma 3.11 to individual states, and the equality in Lemma 3.12 was already proved at the level of states. In the proof of Theorem 3.10 we made a sequence of row swaps using Lemma 3.11 corresponding to the longest word $w_0 = s_{r-1}(s_{r-2}s_{r-1})(s_{r-3}\dots s_{r-1})\dots(s_2\dots s_{r-1})(s_1\dots s_{r-1})$ reversing the row types and horizontal boundary colors. Note that this matches the Schützenberger involution $q_{r-1} = t_1(t_2t_1)(t_3t_2t_1)\dots(t_{r-2}\dots t_1)(t_{r-1}\dots t_1)$ where t_i affects the row types and horizontal boundary colors by s_{r-i} . Thus, even the individual rows swaps in the proof of the left-right duality is refined by the Berenstein–Kirillov involutions to individual states.

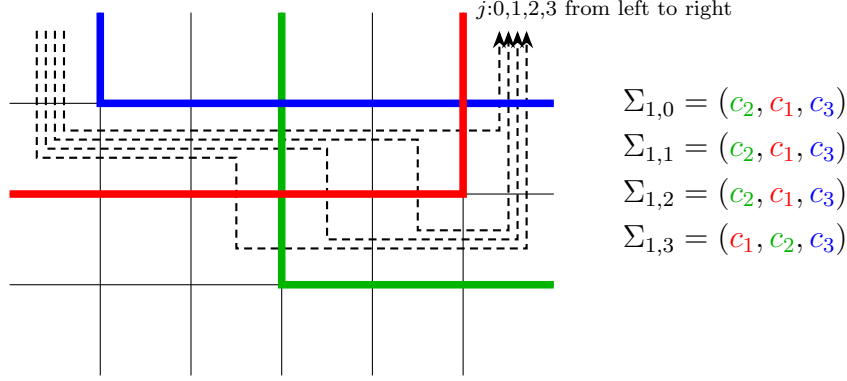


Figure 7. An example of a mixed crystal state with $\Theta = (\Gamma, \Delta, \Gamma)$, $\sigma = (c_3, c_1, c_2)$ along with some of its flags $\Sigma_{1,j}$.

4.3. Proof of Theorem 4.10. Suppose we have some state of a mixed crystal model with row types given by Θ . In the proof we will need to keep track of how the colors of the paths are permuted at various intermediate steps between the global input and output boundary edges. We will call an r -tuple of colors a *flag*. For any i and j satisfying either $0 \leq i < r$ and $0 \leq j \leq N$ or $i = r$ and $j = 0$, consider the subsection of the lattice consisting of the first i rows, along with the left-most j vertices from the next row if this next row is of type Γ and the right-most j vertices from the next row if it is a Δ row. Then define $\Sigma_{i,j}$ to be the flag consisting of the colors of the occupied edges on the output boundary of this subsection in counterclockwise order. See Figure 7 for an example. Note that we have $\Sigma_{i,N} = \Sigma_{i+1,0}$ for every $0 \leq i < r$.

We will use Σ_i as short for $\Sigma_{i,0}$. Note that Σ_0 and Σ_r records the colors of the occupied edges on the input and output boundary, respectively, of the entire lattice. Furthermore, Σ_r and σ determine each other, and in particular if $\Theta = \Delta$ (i.e. left-moving), then $\sigma = \Sigma_r$, and if $\Theta = \Gamma$, then $\sigma = w_0 \Sigma_r$, where w_0 is the longest element in S_r which acts on a flag by reversing it.

Recall from Remark 4.2 that given any uncolored state of a (mixed) crystal model and a coloring of its occupied top edges, there is a unique way to color the remaining occupied edges such that the resulting state becomes admissible. For what follows we need some more details about this unique coloring, namely how $\Sigma_{i,j+1}$ depends on $\Sigma_{i,j}$.

We can see from Table 5 that on a Γ row, when two paths meet, they cross if and only if the left color is larger than the top one. Similarly, we can see from Table 6 that on a Δ row, when two paths meet they cross if and only if the top color is larger than the right one.

Now suppose that we have a coloring of the subsection corresponding to $\Sigma_{i,j}$. By definition, $\Sigma_{i,j+1}$ covers one extra vertex compared to $\Sigma_{i,j}$. If there is only one path that goes through this vertex, then $\Sigma_{i,j+1} = \Sigma_{i,j}$. On the other hand, if two paths meet at this vertex, then

$$(4.13) \quad \Sigma_{i,j+1} = \begin{cases} s_k \Sigma_{i,j} & \text{if } (\Sigma_{i,j})_k > (\Sigma_{i,j})_{k+1} \\ \Sigma_{i,j} & \text{otherwise.} \end{cases}$$

where k is the index of the first of these paths in $\Sigma_{i,j}$ (which means that the other path is indexed by $k+1$) and s_k is the corresponding simple transposition. In the first case the paths cross, in the second they do not. To derive (4.13) note that if the row is of type Δ then the

path of index k in $\Sigma_{i,j}$ corresponds to the top edge and $k+1$ to the right edge while for type Γ they are the left and top edges respectively.

This defines an action of the *Coxeter monoid* \mathbf{S}_r corresponding to the symmetric group S_r , which is the monoid generated by elements $\mathbf{s}_1, \dots, \mathbf{s}_{n-1}$ subject to the relations

$$(4.14) \quad \begin{aligned} \mathbf{s}_i^2 &= \mathbf{s}_i && \text{for all } 1 \leq i < r \\ \mathbf{s}_i \mathbf{s}_{i+1} \mathbf{s}_i &= \mathbf{s}_{i+1} \mathbf{s}_i \mathbf{s}_{i+1} && \text{for all } 1 \leq i < r-1 \\ \mathbf{s}_i \mathbf{s}_j &= \mathbf{s}_j \mathbf{s}_i && \text{when } |i-j| > 1. \end{aligned}$$

Note that it has the same number of generators as S_r and that only the first relation is different. In fact, taking an element with reduced expression $s_{i_1} \dots s_{i_k}$ in S_r to the element $\mathbf{s}_{i_1} \dots \mathbf{s}_{i_k}$ in \mathbf{S}_r gives a well-defined bijection between S_r and \mathbf{S}_r [Tsa90]. In this way we can think of \mathbf{S}_r as having the same elements as S_r but with a different multiplication, known as the *Demazure product*. This monoid is also known as a *0-Hecke monoid* or simply a *Hecke monoid*, because the additive inverses of the generators of a degenerate Hecke algebra with $q=0$ generate a Coxeter monoid under multiplication.

Mirroring (4.13), we define an action of \mathbf{S}_r on flags $\mathbf{d} = (d_1, \dots, d_r) \in \mathcal{P}^r$ by

$$(4.15) \quad \mathbf{s}_i \cdot \mathbf{d} = \begin{cases} \mathbf{s}_i \mathbf{d} & \text{if } d_i > d_{i+1} \\ \mathbf{d} & \text{otherwise.} \end{cases}$$

It is not difficult to check that this indeed is an action of \mathbf{S}_r . We can then rewrite (4.13) as

$$\Sigma_{i,j+1} = \mathbf{s}_k \Sigma_{i,j}.$$

In this way each vertex of type \mathbf{a}_2 or \mathbf{a}'_2 corresponds to acting on the flag with a certain generator \mathbf{s}_k of the Coxeter monoid.

Example 4.11. For the state in Figure 7, the vertices of type \mathbf{a}_2 and \mathbf{a}'_2 correspond to the following equalities

$$\begin{aligned} \Sigma_{0,3} &= \mathbf{s}_1 \Sigma_{0,2} \\ \Sigma_{0,5} &= \mathbf{s}_2 \Sigma_{0,4} \\ \Sigma_{1,3} &= \mathbf{s}_1 \Sigma_{1,2}, \end{aligned}$$

and $\Sigma_{i,j+1}$ is equal to $\Sigma_{i,j}$ in all other cases.

We can also express this in terms of the Gelfand–Tsetlin pattern. Recall that a Γ row-pair is left-strict, and is therefore of the following form:

$$\left\{ \begin{array}{ccccccc} x_0 & & x_1 & & x_k & & x_{k+1} \\ & \searrow & & \nearrow & \searrow & & \nearrow \\ & & y_0 & & y_1 & \dots & y_k \end{array} \right\}.$$

The \mathbf{a}_2 and \mathbf{a}'_2 vertices in the lattice model correspond to non-strict inequalities that are actually equalities in the Gelfand–Tsetlin pattern. We will therefore decorate the Gelfand–Tsetlin pattern by highlighting these equalities, and we will also identify them with monoid generators as follows:

$$(4.16) \quad \left\{ \begin{array}{ccccccc} x_0 & & x_1 & & x_k & & x_{k+1} \\ & \searrow & & \nearrow & \searrow & & \nearrow \\ & & \boxed{\mathbf{s}_{l+1}} & & y_1 & \dots & y_k \end{array} \right\},$$

where l is the number of Δ row-pairs above this one (i.e. the number of paths on the left boundary above this row). Then the flags Σ_{i+1} and Σ_i are related via the action of the highlighted monoid generators, applied sequentially from left to right, i.e.

$$\Sigma_{i+1} = \mathbf{s}_{l+k+1} \cdots \mathbf{s}_{l+1} \Sigma_i.$$

On the other hand, a Δ row-pair is right-strict and has the following form:

$$\left\{ \begin{array}{ccccccc} x_0 & & x_1 & & x_k & & x_{k+1} \\ & \rightrightarrows & & \rightrightarrows & \cdots & \rightrightarrows & \\ & y_0 & & y_1 & & y_k & \end{array} \right\}$$

which we can decorate analogously:

$$(4.17) \quad \left\{ \begin{array}{ccccccc} x_0 & & x_1 & & x_k & & x_{k+1} \\ & \boxed{\mathbf{s}_{l+1}} & & \mathbf{s}_{l+2} & \cdots & \boxed{\mathbf{s}_{l+k+1}} & \\ & y_0 & & y_1 & & y_k & \end{array} \right\},$$

where again l is the number of Δ row-pairs above this one. Then, similarly to the Γ case, the flags Σ_{i+1} and Σ_i are related via the action of the highlighted monoid generators, applied sequentially from *right to left*, i.e.

$$\Sigma_{i+1} = \mathbf{s}_{l+1} \cdots \mathbf{s}_{l+k+1} \Sigma_i.$$

If we include all the inequalities in an entire Gelfand–Tsetlin pattern it would be very large, so we will usually shrink these diagrams to only include the simple transpositions, with an arrow to record in which order the monoid generators should be read as a word (i.e. the opposite order of how they should be applied sequentially). For example, (4.16) would become

$$\left\{ \boxed{\mathbf{s}_{l+1}} \mathbf{s}_{l+2} \cdots \boxed{\mathbf{s}_{l+k+1}} \leftarrow \right\}$$

and (4.17) would become

$$\left\{ \boxed{\mathbf{s}_{l+1}} \cdots \boxed{\mathbf{s}_{l+k+1}} \rightarrow \right\}.$$

Example 4.12. The Gelfand–Tsetlin pattern corresponding to the state in Figure 7 is

$$(4.18) \quad \left\{ \begin{array}{cccc} 4 & & 2 & 0 \\ & 2 & & 0 \\ & & 2 & \end{array} \right\}.$$

The corresponding pattern of simple transpositions is (where we combine the two arrows to a single curved arrow):

$$(4.19) \quad \left\{ \begin{array}{cc} \boxed{\mathbf{s}_1} & \boxed{\mathbf{s}_2} \\ \boxed{\mathbf{s}_1} & \end{array} \curvearrowright \right\},$$

which gives us the following equalities

$$\begin{aligned} \Sigma_1 &= \mathbf{s}_2 \mathbf{s}_1 \Sigma_0 \\ \Sigma_2 &= \mathbf{s}_1 \Sigma_1. \end{aligned}$$

Now suppose that we have some mixed state $\mathfrak{s} \in \mathfrak{S}_{\lambda+\rho}^\Theta$ and let i be such that $\Theta_i \neq \Theta_{i+1}$. This means that we can apply t_{r-i} to \mathfrak{s} , and what we want to show is that the boundary

colors of $t_{r-i}(\mathfrak{s})$ are given by $s_i\sigma$. By the definition of Σ_r , this is equivalent to showing that Σ_r is the same for both \mathfrak{s} and $t_{r-i}(\mathfrak{s})$.

Since the top boundary is the same in both cases, it is enough to show that the two elements in the Coxeter monoid \mathbf{S}_r taking Σ_0 to Σ_r are equal. These elements can be computed from the corresponding Gelfand–Tsetlin patterns, \mathfrak{T} and $t_{r-i}(\mathfrak{T})$. Since the patterns can only differ on row i and we are only interested in the inequalities between the rows, we only need to consider the short patterns \mathfrak{t} and $t_{\text{short}}(\mathfrak{t})$ consisting of rows $i-1$, i and $i+1$. If we can show that the two elements of \mathbf{S}_r corresponding to \mathfrak{t} and $t_{\text{short}}(\mathfrak{t})$ are equal we are done, as the pre- and post-factors corresponding to the rows below and above the short patterns are automatically equal.

A Δ row followed by a Γ row can be described by a short pattern of the following form involving rows $i-1$, i and $i+1$:

$$(4.20) \quad \left\{ \begin{array}{ccccccccccc} x_0 & & & x_1 & & & x_2 & \cdots & x_{k+1} & & & x_{k+2} \\ & \supseteq & & \supsetneq & & \supseteq & \supsetneq & & \supseteq & & \supsetneq & \\ & & y_0 & & & & y_1 & & \cdots & & & y_{k+1} \\ & & & \supsetneq & & \supsetneq & \supsetneq & & \supsetneq & & \supsetneq & \\ & & & & z_0 & & & z_1 & \cdots & & z_k & \end{array} \right\}.$$

Similarly, a Γ row followed by a Δ row can be described by a short pattern of the following form:

$$(4.21) \quad \left\{ \begin{array}{ccccccccccc} x_0 & & & x_1 & & & x_2 & \cdots & x_{k+1} & & & x_{k+2} \\ & \supsetneq & & \supsetneq & & \supsetneq & \supsetneq & & \supsetneq & & \supsetneq & \\ & & y_0 & & & & y_1 & & \cdots & & & y_{k+1} \\ & & & \supseteq & & \supseteq & \supseteq & & \supseteq & & \supseteq & \\ & & & & z_0 & & & z_1 & \cdots & & z_k & \end{array} \right\}.$$

The map t_{short} is a bijection between the sets of these short patterns, and since it is an involution we may without loss of generality assume that \mathfrak{t} is of the first kind. Note that t_{short} will only change the middle row, and we can therefore denote the entries of \mathfrak{t} by x_i , y_i and z_i and the entries of $t_{\text{short}}(\mathfrak{t})$ by x_i , y'_i and z_i .

Now decorate both \mathfrak{t} and $t_{\text{short}}(\mathfrak{t})$ as before and remove everything except the monoid generators \mathbf{s}_k , which gives us patterns of the following forms shown here with example highlights:

$$(4.22) \quad \mathfrak{p}_\Gamma^\Delta = \left\{ \begin{array}{ccccccc} \mathbf{s}_{l+1} & \mathbf{s}_{l+2} & \mathbf{s}_{l+3} & \cdots & \mathbf{s}_{l+k} & \mathbf{s}_{l+k+1} & \mathbf{s}_{l+k+2} \\ & & \mathbf{s}_{l+2} & \mathbf{s}_{l+3} & & \mathbf{s}_{l+k} & \mathbf{s}_{l+k+1} & \mathbf{s}_{l+k+2} \end{array} \right\}$$

and

$$(4.23) \quad \mathfrak{p}_\Delta^\Gamma = \left\{ \begin{array}{ccccccc} \mathbf{s}_{l+1} & \mathbf{s}_{l+2} & \mathbf{s}_{l+3} & \cdots & \mathbf{s}_{l+k} & \mathbf{s}_{l+k+1} & \mathbf{s}_{l+k+2} \\ \mathbf{s}_{l+1} & \mathbf{s}_{l+2} & \mathbf{s}_{l+3} & & \mathbf{s}_{l+k} & \mathbf{s}_{l+k+1} & \end{array} \right\},$$

where l is the number of Δ rows above row i .

Note that in the case $i = r-1$, the last rows of (4.20) and (4.21) do not exist and therefore the resulting patterns in (4.22) and (4.23) would only consist of a single column with only the top generator.

With this notation, the proof of Theorem 4.10 reduces to proving that the element in \mathbf{S}_r obtained by taking the product of the highlighted elements in the order indicated by the arrow is the same for both \mathbf{p}_Γ^Δ and \mathbf{p}_Δ^Γ .

Since the submonoid generated by $\mathbf{s}_{l+1}, \mathbf{s}_{l+2}, \dots, \mathbf{s}_{l+k+2}$ is isomorphic to the one generated by $\mathbf{s}_1, \mathbf{s}_2, \dots, \mathbf{s}_{k+2}$, we can, without loss of generality, assume that $l = 0$.

Blocks: Note that a column where neither of the \mathbf{s}_i are highlighted splits the pattern into two parts, where everything on the left commutes with everything on the right. Furthermore, if the i^{th} column in \mathbf{p}_Γ^Δ is such a column, then so is the i^{th} column in \mathbf{p}_Δ^Γ . To see this, note that if neither \mathbf{s}_i is highlighted in \mathbf{p}_Γ^Δ , then $\min(x_i, z_{i-1}) > y_i$ and therefore $y'_i > \max(x_{i+1}, z_i)$, which means that neither \mathbf{s}_i is highlighted in \mathbf{p}_Δ^Γ .

The columns with no highlighted entries therefore splits \mathbf{p}_Γ^Δ and \mathbf{p}_Δ^Γ into *blocks*, such that any two elements in different blocks commute and the blocks in \mathbf{p}_Γ^Δ and \mathbf{p}_Δ^Γ cover the same columns.

Example 4.13. The following pattern consists of three blocks:

$$\left\{ \begin{array}{ccccccccc} \mathbf{s}_1 & \mathbf{s}_2 & \mathbf{s}_3 & \mathbf{s}_4 & \mathbf{s}_5 & \mathbf{s}_6 & \mathbf{s}_7 & \mathbf{s}_8 & \mathbf{s}_9 \\ & \mathbf{s}_2 & \mathbf{s}_3 & \mathbf{s}_4 & \mathbf{s}_5 & \mathbf{s}_6 & \mathbf{s}_7 & \mathbf{s}_8 & \mathbf{s}_9 \end{array} \right\}$$

Block 1
Block 2
Block 3

and after applying t_{short} we obtain another pattern with blocks in the same columns:

$$\left\{ \begin{array}{ccccccccc} \mathbf{s}_1 & \mathbf{s}_2 & \mathbf{s}_3 & \mathbf{s}_4 & \mathbf{s}_5 & \mathbf{s}_6 & \mathbf{s}_7 & \mathbf{s}_8 & \mathbf{s}_9 \\ \mathbf{s}_1 & \mathbf{s}_2 & \mathbf{s}_3 & \mathbf{s}_4 & \mathbf{s}_5 & \mathbf{s}_6 & \mathbf{s}_7 & \mathbf{s}_8 & \end{array} \right\}$$

Block 1
Block 2
Block 3

Lemma 4.14. Let i be such that column i and $i + 1$ are both inside a single block. Then the highlighting pattern in column i of \mathbf{p}_Δ^Γ is determined by that in column $i + 1$ in \mathbf{p}_Γ^Δ as follows:

- (i) if both of the \mathbf{s}_{i+1} are highlighted in \mathbf{p}_Γ^Δ , then the same is true for the \mathbf{s}_i in \mathbf{p}_Δ^Γ ;
- (ii) if only the top \mathbf{s}_{i+1} is highlighted in \mathbf{p}_Γ^Δ , then only the bottom \mathbf{s}_i is highlighted in \mathbf{p}_Δ^Γ ;
- (iii) if only the bottom \mathbf{s}_{i+1} is highlighted in \mathbf{p}_Γ^Δ , then only the top \mathbf{s}_i is highlighted in \mathbf{p}_Δ^Γ .

Proof. First note that since column $i + 1$ is inside a block, these three cases cover all possibilities.

If we are in case (ii), i.e. only the top \mathbf{s}_{i+1} is highlighted in \mathbf{p}_Γ^Δ , then we must have $y_{i+1} = x_{i+1} < z_i$. Now since column i is also inside a block, at least one of the \mathbf{s}_i in \mathbf{p}_Δ^Γ must be highlighted and therefore $y'_i = \max(x_{i+1}, z_i) = z_i$, which means that only the bottom \mathbf{s}_i is highlighted in \mathbf{p}_Δ^Γ .

The other two cases are similar. □

Lemma 4.14 tells us that \mathbf{p}_Γ^Δ and \mathbf{p}_Δ^Γ almost determine each other, except for the left-most column of the blocks in \mathbf{p}_Γ^Δ and the right-most column of the blocks in \mathbf{p}_Δ^Γ . However, every way of highlighting these columns (such that at least one entry is highlighted) is equivalent. To see this, first note that the left-most column of a block in \mathbf{p}_Γ^Δ has at least one highlighted entry. The elements in this column also commute with every highlighted entry to the left, and we can therefore write them next to each other in the product. Then, because of the quadratic relation $\mathbf{s}_i^2 = \mathbf{s}_i$ in \mathbf{S}_r , all three possible highlighting patterns (top, bottom, both)

are equivalent. We can therefore assume that only the top entry is highlighted, and to remember this special property of the left-most column in a block in \mathbf{p}_Γ^Δ we will remove the bottom entry. We will do the same thing with the right-most column of the blocks in \mathbf{p}_Δ^Γ .

Example 4.15. In Example 4.13, the patterns would become

$$\left\{ \begin{array}{cccccccccc} \boxed{s_1} & s_2 & \boxed{s_3} & s_4 & \boxed{s_5} & s_6 & s_7 & \boxed{s_8} & \boxed{s_9} \\ & \boxed{s_2} & \boxed{s_3} & s_4 & \boxed{s_5} & s_6 & s_7 & \boxed{s_8} & \boxed{s_9} \end{array} \right\} \rightarrow \left\{ \begin{array}{cccccccccc} \boxed{s_1} & s_2 & \boxed{s_3} & s_4 & \boxed{s_5} & s_6 & s_7 & \boxed{s_8} & \boxed{s_9} \\ & \boxed{s_2} & \boxed{s_3} & s_4 & & s_6 & s_7 & & \boxed{s_9} \end{array} \right\}$$

and

$$\left\{ \begin{array}{cccccccccc} \boxed{s_1} & \boxed{s_2} & \boxed{s_3} & s_4 & \boxed{s_5} & \boxed{s_6} & s_7 & \boxed{s_8} & \boxed{s_9} \\ s_1 & \boxed{s_2} & \boxed{s_3} & s_4 & \boxed{s_5} & s_6 & s_7 & \boxed{s_8} & \end{array} \right\} \rightarrow \left\{ \begin{array}{cccccccccc} \boxed{s_1} & \boxed{s_2} & \boxed{s_3} & s_4 & \boxed{s_5} & \boxed{s_6} & s_7 & \boxed{s_8} & \boxed{s_9} \\ s_1 & \boxed{s_2} & & s_4 & \boxed{s_5} & & s_7 & \boxed{s_8} & \end{array} \right\}.$$

The idea now is to step-by-step transform \mathbf{p}_Γ^Δ into \mathbf{p}_Δ^Γ in such a way that the corresponding product in \mathbf{S}_r is preserved at each step.

For these intermediate steps we will need to generalize the patterns above to patterns of the following form:

$$\left\{ \begin{array}{ccccccc} \boxed{s_1} & \boxed{s_2} & \dots & \boxed{s_{i-1}} & \boxed{s_i} & \boxed{s_{i+1}} & \dots & \boxed{s_{k+2}} \\ \boxed{s_1} & \boxed{s_2} & \dots & \boxed{s_{i-1}} & & \boxed{s_{i+1}} & \dots & \boxed{s_{k+2}} \end{array} \right\}.$$

The corresponding element of \mathbf{S}_r is obtained by taking the product of the highlighted entries on the second row inwards towards the arrows, then the central entry (if it is highlighted), and finally the highlighted entries on the first row outwards, away from the arrows. Note that it does not matter if we start by multiplying all highlighted entries on the left-hand side of the second row and then all highlighted entries on the right-hand side, or if we start with the right-hand side and continue with the left-hand side, or if we alternate in some fashion, as every element on the left-hand side commute with every element on the right-hand side.

Example 4.16. The element of \mathbf{S}_6 corresponding to

$$\left\{ \begin{array}{ccccc} \boxed{s_1} & \boxed{s_2} & & \boxed{s_4} & \boxed{s_5} \\ \boxed{s_1} & \boxed{s_2} & & \boxed{s_4} & \boxed{s_5} \end{array} \right\}$$

can be computed in either of the following equivalent ways

$$\begin{aligned} & s_1 s_4 s_3 s_2 s_5 \\ &= s_1 s_4 s_3 s_5 s_2 \\ &= s_4 s_1 s_3 s_2 s_5 \\ &= s_4 s_1 s_3 s_5 s_2. \end{aligned}$$

The patterns \mathbf{p}_Γ^Δ and \mathbf{p}_Δ^Γ can also be written in this form:

$$\mathbf{p}_\Gamma^\Delta = \left\{ \begin{array}{ccccccc} \boxed{s_1} & \boxed{s_2} & \dots & \boxed{s_{k+1}} & \boxed{s_{k+2}} \\ & \boxed{s_2} & & \boxed{s_{k+1}} & \boxed{s_{k+2}} \end{array} \right\} = \left\{ \begin{array}{ccccccc} \boxed{s_1} & \boxed{s_2} & \dots & \boxed{s_{k+1}} & \boxed{s_{k+2}} \\ \boxed{s_1} & \boxed{s_2} & & \boxed{s_{k+1}} & \boxed{s_{k+2}} \end{array} \right\}$$

and

$$\mathbf{p}_\Delta^\Gamma = \left\{ \begin{array}{cccc} \mathbf{s}_1 & \mathbf{s}_2 & \dots & \mathbf{s}_{k+1} \quad \mathbf{s}_{k+2} \\ \mathbf{s}_1 & \mathbf{s}_2 & & \mathbf{s}_{k+1} \end{array} \right\} = \left\{ \begin{array}{cccc} \mathbf{s}_1 & \mathbf{s}_2 & \dots & \mathbf{s}_{k+1} \\ \mathbf{s}_1 & \mathbf{s}_2 & & \mathbf{s}_{k+1} \end{array} \right\} \mathbf{s}_{k+2}.$$

The algorithm transforming \mathbf{p}_Γ^Δ into \mathbf{p}_Δ^Γ while preserving the corresponding product in \mathbf{S}_r can then be described as follows.

Algorithm 4.17. We start with some block of the following shape:

$$\mathbf{p}_\Gamma^\Delta = \left\{ \begin{array}{cccc} \mathbf{s}_1 & \mathbf{s}_2 & \dots & \mathbf{s}_{i-1} \\ \mathbf{s}_1 & \mathbf{s}_2 & \dots & \mathbf{s}_{i-1} \end{array} \right\} \mathbf{s}_i \left\{ \begin{array}{cccc} \mathbf{s}_{i+1} & \mathbf{s}_{i+2} & \dots & \mathbf{s}_n \\ \mathbf{s}_{i+1} & \mathbf{s}_{i+2} & \dots & \mathbf{s}_n \end{array} \right\}$$

for some i (initially $i = 1$).

If \mathbf{s}_i is highlighted, then there are four possibilities for what the i^{th} and $(i+1)^{\text{th}}$ column can look like:

- (i) $\left\{ \begin{array}{cc} \mathbf{s}_i & \mathbf{s}_{i+1} \\ \mathbf{s}_i & \mathbf{s}_{i+1} \end{array} \right\}$ in which case we can replace it with $\left\{ \begin{array}{cc} \mathbf{s}_i & \mathbf{s}_{i+1} \\ \mathbf{s}_i & \mathbf{s}_{i+1} \end{array} \right\}$ using the braid relation $\mathbf{s}_{i+1}\mathbf{s}_i\mathbf{s}_{i+1} = \mathbf{s}_i\mathbf{s}_{i+1}\mathbf{s}_i$;
- (ii) $\left\{ \begin{array}{cc} \mathbf{s}_i & \mathbf{s}_{i+1} \\ \mathbf{s}_i & \mathbf{s}_{i+1} \end{array} \right\}$ in which case we can trivially replace it with $\left\{ \begin{array}{cc} \mathbf{s}_i & \mathbf{s}_{i+1} \\ \mathbf{s}_i & \mathbf{s}_{i+1} \end{array} \right\}$;
- (iii) $\left\{ \begin{array}{cc} \mathbf{s}_i & \mathbf{s}_{i+1} \\ \mathbf{s}_i & \mathbf{s}_{i+1} \end{array} \right\}$ in which case we can trivially replace it with $\left\{ \begin{array}{cc} \mathbf{s}_i & \mathbf{s}_{i+1} \\ \mathbf{s}_i & \mathbf{s}_{i+1} \end{array} \right\}$;
- (iv) $\left\{ \begin{array}{cc} \mathbf{s}_i & \mathbf{s}_{i+1} \\ \mathbf{s}_i & \mathbf{s}_{i+1} \end{array} \right\}$ in which case we can trivially replace it with $\left\{ \begin{array}{cc} \mathbf{s}_i & \mathbf{s}_{i+1} \\ \mathbf{s}_i & \mathbf{s}_{i+1} \end{array} \right\}$.

On the other hand, if \mathbf{s}_i is not highlighted, then there are two possibilities:

- (v) $\left\{ \begin{array}{cc} \mathbf{s}_i & \mathbf{s}_{i+1} \\ \mathbf{s}_i & \mathbf{s}_{i+1} \end{array} \right\}$ in which case we can trivially replace it with $\left\{ \begin{array}{cc} \mathbf{s}_i & \mathbf{s}_{i+1} \\ \mathbf{s}_i & \mathbf{s}_{i+1} \end{array} \right\}$;
- (vi) $\left\{ \begin{array}{cc} \mathbf{s}_i & \mathbf{s}_{i+1} \\ \mathbf{s}_i & \mathbf{s}_{i+1} \end{array} \right\}$ in which case we can trivially replace it with $\left\{ \begin{array}{cc} \mathbf{s}_i & \mathbf{s}_{i+1} \\ \mathbf{s}_i & \mathbf{s}_{i+1} \end{array} \right\}$.

If $i = n - 1$ we are finished. Otherwise, repeat from the beginning with i replaced by $i + 1$.

Example 4.18. For $\left\{ \begin{array}{ccccc} \mathbf{s}_1 & \mathbf{s}_2 & \mathbf{s}_3 & \mathbf{s}_4 & \mathbf{s}_5 \\ \mathbf{s}_2 & \mathbf{s}_3 & \mathbf{s}_4 & \mathbf{s}_5 & \mathbf{s}_5 \end{array} \right\}$ the steps are as follows:

$$\begin{aligned} \left\{ \begin{array}{ccccc} \mathbf{s}_1 & \mathbf{s}_2 & \mathbf{s}_3 & \mathbf{s}_4 & \mathbf{s}_5 \\ \mathbf{s}_2 & \mathbf{s}_3 & \mathbf{s}_4 & \mathbf{s}_5 & \mathbf{s}_5 \end{array} \right\} &= \left\{ \begin{array}{ccccc} \mathbf{s}_1 & \mathbf{s}_2 & \mathbf{s}_3 & \mathbf{s}_4 & \mathbf{s}_5 \\ \mathbf{s}_1 & \mathbf{s}_2 & \mathbf{s}_3 & \mathbf{s}_4 & \mathbf{s}_5 \end{array} \right\} = \left\{ \begin{array}{ccccc} \mathbf{s}_1 & \mathbf{s}_2 & \mathbf{s}_3 & \mathbf{s}_4 & \mathbf{s}_5 \\ \mathbf{s}_1 & \mathbf{s}_2 & \mathbf{s}_3 & \mathbf{s}_4 & \mathbf{s}_5 \end{array} \right\} \\ &= \left\{ \begin{array}{ccccc} \mathbf{s}_1 & \mathbf{s}_2 & \mathbf{s}_3 & \mathbf{s}_4 & \mathbf{s}_5 \\ \mathbf{s}_1 & \mathbf{s}_2 & \mathbf{s}_3 & \mathbf{s}_4 & \mathbf{s}_5 \end{array} \right\} = \left\{ \begin{array}{ccccc} \mathbf{s}_1 & \mathbf{s}_2 & \mathbf{s}_3 & \mathbf{s}_4 & \mathbf{s}_5 \\ \mathbf{s}_1 & \mathbf{s}_2 & \mathbf{s}_3 & \mathbf{s}_4 & \mathbf{s}_5 \end{array} \right\}, \end{aligned}$$

and so the resulting pattern is $\left\{ \begin{array}{ccccc} \mathbf{s}_1 & \mathbf{s}_2 & \mathbf{s}_3 & \mathbf{s}_4 & \mathbf{s}_5 \\ \mathbf{s}_1 & \mathbf{s}_2 & \mathbf{s}_3 & \mathbf{s}_4 & \end{array} \right\}.$

Note that the result of the algorithm is a pattern of the same form as \mathbf{p}_Δ^Γ , and that the \mathbf{s}_i -column was determined by the \mathbf{s}_{i+1} -column in \mathbf{p}_Γ^Δ . Furthermore, when the i^{th} and $(i+1)^{\text{th}}$ columns are inside a block, cases (i) to (iii) above exactly match cases (i) to (iii) in Lemma 4.14. The remaining cases, (iv) describe what happens at the end of a block, (vi) at the beginning of a block, and (v) between blocks and agree with how blocks are treated in connection with Lemma 4.14.

To summarize, the algorithm has step-by-step transformed \mathbf{p}_Γ^Δ to \mathbf{p}_Δ^Γ while preserving the associated element in \mathbf{S}_r . We have thus proved the following proposition:

Proposition 4.19. *The elements of \mathbf{S}_r associated to \mathbf{p}_Γ^Δ and \mathbf{p}_Δ^Γ are the same, and hence the boundary conditions of $t_{r-i}(\mathfrak{s})$ are the same as those of \mathfrak{s} but with row i and $i+1$ switched.*

This concludes the proof of Theorem 4.10.

APPENDIX A. PROOF OF PROPOSITION 3.4

In this appendix we prove that the mixed R -matrices $R_R^L : V_L \otimes V_R \rightarrow V_R \otimes V_L$ and $R_L^R : V_R \otimes V_L \rightarrow V_L \otimes V_R$ from Table 8 satisfy $R_R^L R_L^R = C \cdot \mathbb{1}_{V_R} \otimes \mathbb{1}_{V_L}$ for some constant C depending on q, z_1, z_2 and the palette size m . Since V_L and V_R are finite-dimensional modules over the field of rational functions in q, z_1 and z_2 for a fixed integer m , this means that $R_L^R R_R^L = C \cdot \mathbb{1}_{V_L} \otimes \mathbb{1}_{V_R}$ as well. Indeed, let $A = \frac{1}{C} R_L^R \tau$ and $B = \tau R_R^L$ where τ is the linear map defined on pure tensors by $u \otimes v \mapsto v \otimes u$. Then $A, B \in \text{End}(V_L \otimes V_R)$ and the left-inverse A of B is also the right-inverse of B .

The weights in Table 8 assume that the R -vertices attach to left of rows with row parameters z_1 above z_2 and an R -vertex swaps these row parameters. Thus we actually want to show that

$$(A.1) \quad R_R^L(z_2, z_1) R_L^R(z_1, z_2) = (z_2 - q^2 z_1)(z_2 - q^{2m} z_1) \mathbb{1}_{V_R} \otimes \mathbb{1}_{V_L}.$$

Both R -vertices have the same vertex color c_k . Due to the fact that the weights only depend on the possible edge colors c_i and c_j by expressions in $i - k$ and $j - k \pmod m$ we may without loss of generality assume that $k = 1$. Indeed, the conditions $\left\{ \begin{smallmatrix} i < j < k \text{ or } j < k \leq i \text{ or } k \leq i < j \\ j < i < k \text{ or } i < k \leq j \text{ or } k \leq j < i \end{smallmatrix} \right\}$ are equivalent to $\text{res}_m(i - j) - \text{res}_m(i - k) + \text{res}_m(j - k) = \left\{ \begin{smallmatrix} m \\ 0 \end{smallmatrix} \right\}$.

We first enumerate the possible admissible states using the configurations of Table 8, starting from the possible left boundary edges and iteratively filling in the rest. Here, dashed edges signify unknown edges and the equations should be interpreted as equalities and unions of sets of states.

$$\begin{aligned}
 & \begin{array}{c} R_R^L \quad R_L^R \\ \text{Diagram 1} \end{array} = \begin{array}{c} \text{Diagram 2} \end{array} + \sum_i \begin{array}{c} \text{Diagram 3} \end{array} \\
 & = \begin{array}{c} \text{Diagram 4} \end{array} + \sum_j \begin{array}{c} \text{Diagram 5} \end{array} + \sum_i \begin{array}{c} \text{Diagram 6} \end{array} + \sum_{i,j} \begin{array}{c} \text{Diagram 7} \end{array} \\
 & \begin{array}{c} \text{Diagram 8} \end{array} = \begin{array}{c} \text{Diagram 9} \end{array} + \sum_l \begin{array}{c} \text{Diagram 10} \end{array} \\
 & = \begin{array}{c} \text{Diagram 11} \end{array} + \sum_j \begin{array}{c} \text{Diagram 12} \end{array} + \sum_l \begin{array}{c} \text{Diagram 13} \end{array} + \sum_{j,l} \begin{array}{c} \text{Diagram 14} \end{array} \\
 & \begin{array}{c} \text{Diagram 15} \end{array} = \begin{array}{c} \text{Diagram 16} \end{array} = \begin{array}{c} \text{Diagram 17} \end{array} \\
 & \begin{array}{c} \text{Diagram 18} \end{array} = \begin{array}{c} \text{Diagram 19} \end{array} = \begin{array}{c} \text{Diagram 20} \end{array} \\
 & \begin{array}{c} \text{Diagram 21} \end{array} = \begin{array}{c} \text{Diagram 22} \end{array} = \begin{array}{c} \text{Diagram 23} \end{array} \quad (i \neq j)
 \end{aligned}$$

Let us now consider the weights. It remains to show that when the left and right boundary edges match (from top to bottom) then the corresponding partition function, summing

over all admissible internal edge configurations, is equal to $(z_2 - q^2 z_1)(z_2 - q^{2m} z_1)$ and that otherwise the partition function is zero.

Using the weights from Table 8 we immediately get that

$$\begin{aligned} Z \left(\begin{array}{c} \text{Diagram 1: A diamond shape with two internal vertices. The top and bottom edges are red, and the left and right edges are black. The top and bottom vertices are labeled with red 'i' and the left and right vertices are labeled with black 'i' in italics.} \end{array} \right) = Z \left(\begin{array}{c} \text{Diagram 2: A diamond shape with two internal vertices. The top and bottom edges are red, and the left and right edges are black. The top and bottom vertices are labeled with red 'i' and the left and right vertices are labeled with black 'i' in italics.} \end{array} \right) = \Phi(z_2 - q^2 z_1) \cdot (z_2 - q^{2m} z_1) / \Phi = C \\ Z \left(\begin{array}{c} \text{Diagram 3: A diamond shape with two internal vertices. The top and bottom edges are red, and the left and right edges are blue. The top and bottom vertices are labeled with red 'i' and the left and right vertices are labeled with blue 'j' in italics.} \end{array} \right) = \Phi^2 \mathfrak{X}_{j,i}(z_2 - q^2 z_1) \cdot \frac{\mathfrak{X}_{i,j}}{(q\Phi)^2} (z_2 - q^{2m} z_1) = C \quad (i \neq j)$$

since $\mathfrak{X}_{i,j} \mathfrak{X}_{j,i} = q^2$ for $i \neq j$.

The remaining cases involve sums over internal colors, i.e. color loops, where the sum are over all m colors. That (A.1), and therefore also the Yang–Baxter equations, holds for all m can be explained by the fact that these sums turn out to be telescopic due to an intricate interplay between the two vertex weights in each state.

$$\begin{aligned} Z \left(\begin{array}{c} \text{Diagram 4: A diamond shape with two internal vertices. The top and bottom edges are black, and the left and right edges are black. The top and bottom vertices are labeled with black 'i' and the left and right vertices are labeled with black 'i' in italics.} \end{array} + \sum_i \begin{array}{c} \text{Diagram 5: A diamond shape with two internal vertices. The top and bottom edges are red, and the left and right edges are black. The top and bottom vertices are labeled with red 'i' and the left and right vertices are labeled with black 'i' in italics.} \end{array} \right) = \\ = (z_2 - z_1)(z_2 - q^{2m+2} z_1) + \sum_{i=1}^m \Phi(1 - q^2) z_2 \cdot \frac{1}{\Phi} q^{2 \text{res}_m(i-1)} (1 - q^2) z_1 \\ = (z_2 - z_1)(z_2 - q^{2m+2} z_1) + z_1 z_2 (1 - q^2) \sum_{i=1}^m (1 - q^2) q^{2(i-1)} \\ = (z_2 - z_1)(z_2 - q^{2m+2} z_1) + z_1 z_2 (1 - q^2) (1 - q^{2m}) = C \end{aligned}$$

since $\sum_{i=1}^m (1 - q^2) q^{2(i-1)} = \sum_{i=1}^m (q^{2(i-1)} - q^{2i}) = 1 - q^{2m}$.

For the next computation we first separate the term where $i = j$ and then use the fact that $k = 1$ to simplify the conditions appearing in the weights in Table 8.

$$\begin{aligned} Z \left(\begin{array}{c} \text{Diagram 6: A diamond shape with two internal vertices. The top and bottom edges are blue, and the left and right edges are black. The top and bottom vertices are labeled with blue 'j' and the left and right vertices are labeled with black 'j' in italics.} \end{array} + \sum_i \begin{array}{c} \text{Diagram 7: A diamond shape with two internal vertices. The top and bottom edges are red, and the left and right edges are blue. The top and bottom vertices are labeled with red 'i' and the left and right vertices are labeled with blue 'j' in italics.} \end{array} \right) = Z \left(\begin{array}{c} \text{Diagram 8: A diamond shape with two internal vertices. The top and bottom edges are blue, and the left and right edges are black. The top and bottom vertices are labeled with blue 'j' and the left and right vertices are labeled with black 'j' in italics.} \end{array} + \begin{array}{c} \text{Diagram 9: A diamond shape with two internal vertices. The top and bottom edges are blue, and the left and right edges are blue. The top and bottom vertices are labeled with blue 'j' and the left and right vertices are labeled with blue 'j' in italics.} \end{array} + \sum_{i \neq j} \begin{array}{c} \text{Diagram 10: A diamond shape with two internal vertices. The top and bottom edges are red, and the left and right edges are blue. The top and bottom vertices are labeled with red 'i' and the left and right vertices are labeled with blue 'j' in italics.} \end{array} \right) = \\ = (z_2 - z_1) \cdot \frac{1}{\Phi} q^{2 \text{res}_m(1-j)-2} (1 - q^2) z_2 + \Phi(1 - q^2) z_2 \cdot (q^{2m-2} z_1 - z_2) / \Phi^2 + \\ + \sum_{i \neq j} \Phi(1 - q^2) z_2 \cdot \frac{1}{\Phi^2} q^{2 \text{res}_m(i-j)-2} (1 - q^2) \begin{cases} z_1 & \text{if } i < j \\ z_2 & \text{if } j < i \end{cases} \end{aligned}$$

Since

$$\begin{aligned} \sum_{i \neq j} q^{2 \text{res}_m(i-j)-2} (1 - q^2) \begin{cases} z_1 & \text{if } i < j \\ z_2 & \text{if } j < i \end{cases} &= z_1 \sum_{i < j} q^{2(m+i-j)-2} (1 - q^2) + z_2 \sum_{i > j} q^{2(i-j)-2} (1 - q^2) = \\ &= z_1 (q^{2(m+1-j)-2} - q^{2(m+j-1-j)}) + z_2 (q^{2(j+1-j)-2} - q^{2(m-j)}) \end{aligned}$$

and $\text{res}_m(1-j) = m+1-j$ for $j \in \{1, \dots, m\}$ we get that the partition function equals

$$\frac{1}{\Phi} (1 - q^2) z_2 \left((z_2 - z_1) q^{2(m-j)} + (q^{2m-2} z_1 - z_2) + z_1 (q^{2(m-j)} - q^{2(m-1)}) + z_2 (1 - q^{2(m-j)}) \right) = 0.$$

The mirrored case is similar.

$$\begin{aligned}
Z \left(\begin{array}{c} \text{Diagram 1} \\ + \sum_l \begin{array}{c} \text{Diagram 2} \end{array} \end{array} \right) &= Z \left(\begin{array}{c} \text{Diagram 1} \\ + \begin{array}{c} \text{Diagram 3} \end{array} \\ + \sum_{l \neq i} \begin{array}{c} \text{Diagram 4} \end{array} \end{array} \right) = \\
&= \Phi(1 - q^2)z_1 \cdot (z_2 - q^{2m+2}z_1) + \Phi^2(q^4z_1 - z_2) \cdot \frac{1}{\Phi} q^{2\text{res}_m(i-1)}(1 - q^2)z_1 + \\
&\quad + \sum_{l \neq i} -\Phi^2(1 - q^2) \left\{ \begin{array}{c} q^2 z_1 \text{ if } i < l \\ z_2 \text{ if } l < i \end{array} \right\} \cdot \frac{1}{\Phi} q^{2\text{res}_m(l-1)}(1 - q^2)z_1 \\
&= \Phi(1 - q^2)z_1 \left(z_2 - q^{2m+2}z_1 + (q^4z_1 - z_2)q^{2(i-1)} + \right. \\
&\quad \left. - z_2 \sum_{l < i} (1 - q^2)q^{2(l-1)} - q^2z_1 \sum_{l > i} (1 - q^2)q^{2(l-1)} \right) \\
&= \Phi(1 - q^2)z_1 \left(z_2 - q^{2m+2}z_1 + (q^4z_1 - z_2)q^{2(i-1)} - z_2(1 - q^{2(i-1)}) - q^2z_1(q^{2i} - q^{2m}) \right) = 0.
\end{aligned}$$

Finally, the last remaining partition function is

$$Z \left(\begin{array}{c} \text{Diagram 5} \\ + \sum_l \begin{array}{c} \text{Diagram 6} \end{array} \end{array} \right).$$

We will split this computation into two cases: $i = j$ and $i \neq j$. For $i = j$ we get that the partition function equals

$$\begin{aligned}
Z \left(\begin{array}{c} \text{Diagram 7} \\ + \begin{array}{c} \text{Diagram 8} \end{array} \\ + \sum_{l \neq i} \begin{array}{c} \text{Diagram 9} \end{array} \end{array} \right) &= \\
&= \Phi(1 - q^2)z_1 \cdot \frac{1}{\Phi} q^{2\text{res}_m(1-i)-2}(1 - q^2)z_2 + \Phi^2(q^4z_1 - z_2) \cdot (q^{2m-2}z_1 - z_2)/\Phi^2 + \\
&\quad + \sum_{l \neq i} -\Phi^2(1 - q^2) \left\{ \begin{array}{c} q^2 z_1 \text{ if } i < l \\ z_2 \text{ if } l < i \end{array} \right\} \cdot \frac{1}{\Phi^2} q^{2\text{res}_m(l-i)-2}(1 - q^2) \left\{ \begin{array}{c} z_1 \text{ if } l < i \\ z_2 \text{ if } i < l \end{array} \right\} \\
&= (1 - q^2)z_1 \cdot q^{2(m+1-i)-2}(1 - q^2)z_2 + (q^4z_1 - z_2) \cdot (q^{2m-2}z_1 - z_2) + \\
&\quad - (1 - q^2)z_1z_2 \sum_{l \neq i} (1 - q^2)q^{2\text{res}_m(l-i)-2} \left\{ \begin{array}{c} q^2 \text{ if } i < l \\ 1 \text{ if } l < i \end{array} \right\}
\end{aligned}$$

where we have used that $\text{res}_m^m(1 - i) = m + 1 - i$ for $i \in \{1, \dots, m\}$. We split up the sum into two parts to obtain

$$\begin{aligned}
\sum_{l \neq i} (1 - q^2)q^{2\text{res}_m(l-i)-2} \left\{ \begin{array}{c} q^2 \text{ if } i < l \\ 1 \text{ if } l < i \end{array} \right\} &= \sum_{l < i} (1 - q^2)q^{2(m+l-i)-2} + \sum_{l > i} (1 - q^2)q^{2(l-i)} = \\
&= q^{2(m+1-i)-2} - q^{2(m+i-1-i)} + q^{2(i+1-i)} - q^{2(m-i)+2}.
\end{aligned}$$

Thus we obtain the partition function

$$\begin{aligned}
&= (1 - q^2)z_1 \cdot q^{2(m-i)}(1 - q^2)z_2 + (q^4z_1 - z_2) \cdot (q^{2m-2}z_1 - z_2) + \\
&\quad - (1 - q^2)z_1z_2(q^{2(m-i)} - q^{2(m-1)} + q^2 - q^{2(m-i)+2}) = C.
\end{aligned}$$

For $i \neq j$ we get that the partition function equals

$$\begin{aligned}
Z & \left(\begin{array}{c} \text{Diagram 1: } i \text{ (red) and } j \text{ (blue) crossing at a black dot, with } i \text{ (red) and } j \text{ (blue) lines extending from the dot.} \\ \text{Diagram 2: } i \text{ (red) and } j \text{ (blue) crossing at a black dot, with } i \text{ (red) and } j \text{ (blue) lines extending from the dot.} \\ \text{Diagram 3: } i \text{ (red) and } j \text{ (blue) crossing at a black dot, with } i \text{ (red) and } j \text{ (blue) lines extending from the dot.} \end{array} + \sum_{l \neq i, j} \begin{array}{c} \text{Diagram 4: } i \text{ (red) and } l \text{ (green) crossing at a black dot, with } i \text{ (red) and } l \text{ (green) lines extending from the dot.} \end{array} \right) = \\
& = \Phi(1 - q^2)z_1 \cdot \frac{1}{\Phi} q^{2 \text{res}_m(1-j)-2} (1 - q^2)z_2 + \\
& + \Phi^2(q^4 z_1 - z_2) \cdot \frac{1}{\Phi^2} q^{2 \text{res}_m(i-j)-2} (1 - q^2) \left\{ \begin{array}{l} z_1 \text{ if } i < j \\ z_2 \text{ if } j < i \end{array} \right\} + \\
& - \Phi^2(1 - q^2) \left\{ \begin{array}{l} q^2 z_1 \text{ if } i < j \\ z_2 \text{ if } j < i \end{array} \right\} \cdot (q^{2m-2} z_1 - z_2) / \Phi^2 + \\
& + \sum_{l \neq i, j} -\Phi^2(1 - q^2) \left\{ \begin{array}{l} q^2 z_1 \text{ if } i < l \\ z_2 \text{ if } l < i \end{array} \right\} \cdot \frac{1}{\Phi^2} q^{2 \text{res}_m(l-j)-2} (1 - q^2) \left\{ \begin{array}{l} z_1 \text{ if } l < j \\ z_2 \text{ if } j < l \end{array} \right\} \\
& = (1 - q^2) \left(z_1 q^{2(m-j)} (1 - q^2) z_2 + (q^4 z_1 - z_2) q^{2(i-j)-2} \left\{ \begin{array}{l} q^{2m} z_1 \text{ if } i < j \\ z_2 \text{ if } j < i \end{array} \right\} + \right. \\
& \left. - \left\{ \begin{array}{l} q^2 z_1 \text{ if } i < j \\ z_2 \text{ if } j < i \end{array} \right\} (q^{2m-2} z_1 - z_2) - \underbrace{\sum_{l \neq i, j} \left\{ \begin{array}{l} q^2 z_1 \text{ if } i < l \\ z_2 \text{ if } l < i \end{array} \right\} q^{2(l-j)-2} (1 - q^2) \left\{ \begin{array}{l} q^{2m} z_1 \text{ if } l < j \\ z_2 \text{ if } j < l \end{array} \right\}}_A \right).
\end{aligned}$$

Let us simplify the last sum A . For $i < j$ we split the sum over l into the cases: $l < i < j$, $i < l < j$ and $i < j < l$. We then get that

$$\begin{aligned}
A & \stackrel{i < j}{=} q^{2m-2j-2} z_1 z_2 \sum_{l < i < j} q^{2l} (1 - q^2) + q^{2m-2j} z_1^2 \sum_{i < l < j} q^{2l} (1 - q^2) + q^{-2j} z_1 z_2 \sum_{i < j < l} q^{2l} (1 - q^2) \\
& = q^{2m-2j-2} z_1 z_2 (q^2 - q^{2i}) + q^{2m-2j} z_1^2 (q^{2(i+1)} - q^{2j}) + q^{-2j} z_1 z_2 (q^{2(j+1)} - q^{2m+2}).
\end{aligned}$$

For $j < i$ we split A into the cases: $l < j < i$, $j < l < i$ and $j < i < l$, and get that

$$\begin{aligned}
A & \stackrel{j < i}{=} q^{2m-2j-2} z_1 z_2 \sum_{l < j < i} q^{2l} (1 - q^2) + q^{-2j-2} z_2^2 \sum_{j < l < i} q^{2l} (1 - q^2) + q^{-2j} z_1 z_2 \sum_{j < i < l} q^{2l} (1 - q^2) \\
& = q^{2m-2j-2} z_1 z_2 (q^2 - q^{2j}) + q^{-2j-2} z_2^2 (q^{2(j+1)} - q^{2i}) + q^{-2j} z_1 z_2 (q^{2(i+1)} - q^{2m+2}).
\end{aligned}$$

After collecting all the terms this shows that the partition function is zero for both $i < j$ and $j < i$, and this completes the proof.

REFERENCES

- [BBB19] Ben Brubaker, Valentin Buciumas, and Daniel Bump. A Yang-Baxter equation for metaplectic ice. Appendix ([BBBG17]) joint with Nathan Gray. *Commun. Number Theory Phys.*, 13(1):101–148, 2019.
- [BBBF18] Ben Brubaker, Valentin Buciumas, Daniel Bump, and Solomon Friedberg. Hecke modules from metaplectic ice. *Selecta Math. (N.S.)*, 24(3):2523–2570, 2018.
- [BBBG17] Ben Brubaker, Valentin Buciumas, Daniel Bump, and Nathan Gray. Duality for metaplectic ice (appendix to [BBB19]). 2017, [arXiv:1709.06500](https://arxiv.org/abs/1709.06500).
- [BBBG21] Ben Brubaker, Valentin Buciumas, Daniel Bump, and Henrik P. A. Gustafsson. Colored five-vertex models and Demazure atoms. *J. Combin. Theory Ser. A*, 178:Paper No. 105354, 48, 2021.

- [BBBG24a] Ben Brubaker, Valentin Buciumas, Daniel Bump, and Henrik P. A. Gustafsson. Colored vertex models and Iwahori Whittaker functions. *Selecta Math. (N.S.)*, 30(4):Paper No. 78, 58, 2024.
- [BBBG24b] Ben Brubaker, Valentin Buciumas, Daniel Bump, and Henrik P. A. Gustafsson. Iwahori-metaplectic duality. *J. Lond. Math. Soc. (2)*, 109(6), 2024.
- [BBBG24c] Ben Brubaker, Valentin Buciumas, Daniel Bump, and Henrik P. A. Gustafsson. Metaplectic Iwahori Whittaker functions and supersymmetric lattice models. 2024, [arXiv:2012.15778](#).
- [BBC⁺12] Ben Brubaker, Daniel Bump, Gautam Chinta, Solomon Friedberg, and Paul E. Gunnells. Metaplectic ice. In *Multiple Dirichlet series, L-functions and automorphic forms*, volume 300 of *Progr. Math.*, pages 65–92. Birkhäuser/Springer, New York, 2012.
- [BBF11a] Ben Brubaker, Daniel Bump, and Solomon Friedberg. Schur polynomials and the Yang-Baxter equation. *Comm. Math. Phys.*, 308(2):281–301, 2011.
- [BBF11b] Ben Brubaker, Daniel Bump, and Solomon Friedberg. *Weyl group multiple Dirichlet series: type A combinatorial theory*, volume 175 of *Annals of Mathematics Studies*. Princeton University Press, Princeton, NJ, 2011.
- [BBG25] Ben Brubaker, Daniel Bump, and Henrik P. A. Gustafsson. Quantum superalgebras and the free-fermionic Yang-Baxter equation. 2025, [arXiv:2503.24189](#).
- [BK72] Edward A. Bender and Donald E. Knuth. Enumeration of plane partitions. *J. Combinatorial Theory Ser. A*, 13:40–54, 1972.
- [BN24] Daniel Bump and Slava Naprienko. Colored Bosonic models and matrix coefficients. *Commun. Number Theory Phys.*, 18(2):441–484, 2024.
- [BS22] Valentin Buciumas and Travis Scrimshaw. Quasi-solvable lattice models for Sp_{2n} and SO_{2n+1} Demazure atoms and characters. *Forum Math. Sigma*, 10:Paper No. e53, 34, 2022.
- [BW22] Alexei Borodin and Michael Wheeler. Nonsymmetric Macdonald polynomials via integrable vertex models. *Trans. Amer. Math. Soc.*, 375(12):8353–8397, 2022.
- [Gra17] Nathan Tyler Gray. *Metaplectic Ice for Cartan Type C*. ProQuest LLC, Ann Arbor, MI, 2017. Thesis (Ph.D.)—University of Minnesota.
- [Kas90] Masaki Kashiwara. Crystalizing the q -analogue of universal enveloping algebras. *Comm. Math. Phys.*, 133(2):249–260, 1990.
- [KB95] A. N. Kirillov and A. D. Berenstein. Groups generated by involutions, Gel’fand-Tsetlin patterns, and combinatorics of Young tableaux. *Algebra i Analiz*, 7(1):92–152, 1995.
- [KS97] Anatoli Klimyk and Konrad Schmüdgen. *Quantum groups and their representations*. Texts and Monographs in Physics. Springer-Verlag, Berlin, 1997.
- [Lus90] G. Lusztig. Canonical bases arising from quantized enveloping algebras. *J. Amer. Math. Soc.*, 3(2):447–498, 1990.
- [Nap22] Slava Naprienko. Integrability of the six-vertex model and the Yang-Baxter groupoid, 2022, [arXiv:2210.14883](#).
- [Tsa90] S. V. Tsaranov. Representation and classification of Coxeter monoids. *European J. Combin.*, 11(2):189–204, 1990.

DEPARTMENT OF MATHEMATICS AND MATHEMATICAL STATISTICS, UMEÅ UNIVERSITY, SE-901 87 UMEÅ, SWEDEN

Email address: `henrik.gustafsson@umu.se`

DEPARTMENT OF MATHEMATICS AND MATHEMATICAL STATISTICS, UMEÅ UNIVERSITY, SE-901 87 UMEÅ, SWEDEN

Email address: `carl.westerlund@umu.se`